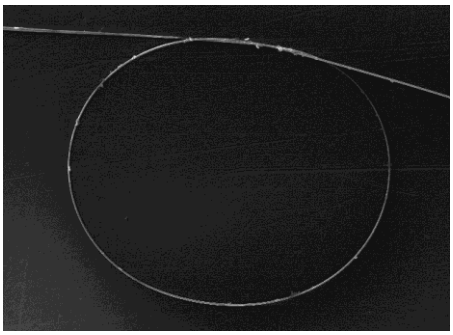

Sensors based on Taper Device for Knot Configuration

André Rodrigues Delgado Coelho Gomes
Integrated Master's in Engineering Physics
Department of Physics and Astronomy
2016

Supervisor
Orlando José dos Reis Frazão, Invited Assistant Professor, Faculty of Sciences of the University of Porto and Senior Researcher, INESC TEC

All modifications determined by the Jury, and only those, were made.

The president of the Jury,

Porto, _____/_____/_____

Acknowledgements

This work would not be possible to write without the contribution and the valuable support of many people who helped me during this journey, of which only to some is possible to give particular mention here.

This dissertation would not have been possible without the help of my supervisor, Dr. Orlando Frazão, whose work, dedication, support, and encouragement to improve my academic record were fundamental. To him my heartfelt thanks for all the dedication and for all the opportunities that he brought me.

I am also very grateful to INESC TEC, more specifically the Center of Applied Photonics, for welcoming me, to all my colleagues for helping me in any way they could to the CORAL project, financed by FCT – Fundação para a Ciência e Tecnologia (Portuguese Foundation for Science and Technology) and by ERDF (European Regional Development Fund) through: COMPETE Programme (Operational Programme for Competitiveness) within project FCOMP-01-0124-FEDER-037281; ON.2 – O Novo Norte (Northern Portugal Regional Operational Programme).

I would like to acknowledge the financial support provided by DAAD (German Academic Exchange Service) through the 5 months scholarship, allowing me to do most of my work abroad. I would also like to thank the Institute for Photonic Technology (IPHT) in Jena, in particular Professor Hartmut Bartelt and Dr. Martin Becker for their indispensable support during the time I spent at the institute. Thanks also go to Adrian Lorenz for his help in teaching me how to use COMSOL Multiphysics, for his support, and opinions.

A special thanks to my colleagues and friends, Ricardo André and Stephen Warren-Smith, for all the assistance, guidance, work, fruitful conversations, and shared experiences. I am also very grateful to Beatriz Silveira for all the work and support in providing optical fiber tapers that were used in some parts of my research work.

Lastly, to my parents for encouraging me and for always supporting my decisions, and to my friends, especially Nuna, Quesado and JP, for supporting and helping me with my worries and problems, and for enduring my conversations about physics.

Abstract

This dissertation explores the study and development of optical fiber sensors based on tapers. The main objective is to explore and design new sensing structures, mainly interferometric and resonating structures based on tapers, for measuring refractive index and temperature with the possibility of performing simultaneous measurement of these two parameters. The dissertation starts with a synthesis of the advances in this area of optical fiber sensing, with a special focus on interferometric and resonating structures using tapers.

The dissertation can be divided into two parts. The first part is the study and development of sensors based on a knot resonator structure. A Mach-Zehnder interferometer is fabricated based on a large knot fiber resonator structure using a taper with almost half the diameter of a single mode fiber. The principle of working of the structure is studied and a characterization in refractive index and temperature is performed. The incorporation of well-known devices, such as fiber Bragg gratings and Fabry-Perot cavities, in microfiber knot resonator structures is explored. A fiber Bragg grating is successfully embedded in the ring region of a microfiber knot resonator. The creation of a Fabry-Perot cavity in a microfiber knot resonator using focused ion beam milling is studied. Two alternative configurations are also presented. The first involves milling two small rips in a microfiber knot resonator creating a silica cavity, which was not explored in this dissertation. The second alternative is the creation of a cavity in the taper region next to the microfiber knot resonator structure. The device was fabricated and some preliminary results in terms of refractive index sensing were obtained. The second part of this dissertation is dedicated to the study of a fiber Bragg grating in an abrupt taper tip. The device is characterized in refractive index and temperature.

In the end, some unexplored parts of this work are analyzed and some future lines of investigation are presented.

Keywords: Optical fiber sensors, fiber tapers, microfiber knot resonator, interferometer, fiber Bragg gratings, focused ion beam.

Resumo

Esta dissertação explora o estudo e desenvolvimento de sensores em fibra óptica baseados em *tapers*. O objectivo principal é explorar e desenhar novas estruturas sensoras, principalmente estruturas interferometricas ou de ressonância baseadas em *tapers*, para medir índice de refração e temperatura com a possibilidade de conseguir medir simultaneamente estes dois parâmetros. Esta dissertação começa com uma síntese dos avanços nesta área de sensorização com fibras ópticas, com especial foco em estruturas interferométricas e de ressonância usando *tapers*.

A dissertação pode ser dividida em duas partes. A primeira parte é o estudo e desenvolvimento de sensores baseados numa estrutura de *knot resonator* (nó ressoador). Um interferómetro de *Mach-Zehnder* é fabricado com base numa estrutura de nó ressoador grande em fibra usando um *taper* com um diâmetro de quase metade do diâmetro de uma fibra *single mode*. O princípio de funcionamento da estrutura é estudado e uma caracterização em índice de refração e temperatura é realizada. A incorporação de dispositivos bem conhecidos, como redes de *Bragg* em fibra e cavidades *Fabry-Perot*, em nós ressoadores de microfibra é explorada. Uma rede de *Bragg* em fibra é embebida com sucesso na região do anel de um nó ressoador em microfibra. A criação de uma cavidade *Fabry-Perot* num nó ressoador em microfibra usando um feixe de iões focado é estudada. Duas configurações alternativas são também apresentadas. A primeira envolve o *milling* de dois pequenos rasgos num nó ressoador em microfibra criando uma cavidade em sílica, o que não foi explorado nesta dissertação. A segunda alternativa é a criação de uma cavidade na região do *taper* ao lado da estrutura do nó ressoador em microfibra. O dispositivo foi fabricado e alguns resultados preliminares em termos de sensorização de índice de refração foram obtidos. A segunda parte desta dissertação é dedicada ao estudo de redes de *Bragg* numa ponta de *taper* abrupto. O dispositivo é caracterizado em índice de refração e temperatura.

No final, algumas partes não exploradas deste trabalho são analisadas e algumas linhas de investigação futura são apresentadas.

Palavras-chave: Sensores em fibra óptica, *tapers* em fibra, *microfiber knot resonator*, interferómetro, redes de Bragg em fibra, feixe de iões focado.

Contents

List of Figures

List of Tables

Nomenclature

FBG – Fiber Bragg Grating
FIB – Focused Ion Beam
FP – Fabry-Perot
FSR – Free Spectral Range
LPG – Long Period Grating
MCR – Micro-Coil Resonator
MKR – Microfiber Knot Resonator
MLR – Microfiber Loop Resonator
MNF – Micro and Nanofibers
MZI – Mach-Zehnder Interferometer
MZ-LKR - Mach-Zehnder based on a Large Knot Fiber Resonator
OSA – Optical Spectrum Analyzer
Q-factor – Quality Factor
RI – Refractive Index
RIU – Refractive Index Units
SMF – Single Mode Fiber

Chapter 1
Introduction

1.1. Motivation

Over the last few decades, optical fiber sensing proved to be one of the most powerful and successful application of both optical fibers and sensing technology [1]. In fact, with the developments and the advances of the telecommunication industry, optical fibers begun to be a subject of intense investigation. With this outbreak, their application to various sensing fields were widely explored until nowadays.

Optical fibers present unique characteristics, fulfilling many requirements that the industry is currently demanding: low cost, reduced size, fast response, electromagnetic compatibility, remote sensing, high flexibility, among others; all combined in one sensor with the possibility of multiple applications [2].

From the combination of optical fibers and nanotechnology, the fabrication of micro and nanofibers (MNF) by tapering a fiber to micrometric or even nanometric size [1] has led optical fiber sensing to another level. With them, new properties were revealed, such as low optical loss, outstanding mechanical flexibilities, tight optical confinement and large interaction with the external medium through their large evanescent field [3]. Moreover, this characteristics can be all joined together to create new miniaturized sensors [1].

Until nowadays, new sensors based on taper configuration were extensively studied and developed. High quality factor resonators [4], [5], functionalized microfibers [6], interferometers [7], [8], are some of the multiple applications of tapers. For instance, a simple biconical fiber taper [9] or a concatenation of two single-mode fiber tapers [7] can create a Mach-Zehnder or a Michelson interferometer [10]. However, if a simple loop [5] or a knot [4] is made in an optical microfiber taper instead, a high Q-resonator can be created.

The Mach-Zehnder interferometer (MZI) was vastly used, mainly as a refractive index sensor [11], but year after year new configurations were developed increasing, therefore, the scope of this sensor. Temperature [12], curvature [13], and others are some of the parameters that began to be measured with new configurations of this sensor. Currently there are still new developments being done in this topic, which now

involves creating new configurations with enhanced sensitivity by combining different structures [14], [15].

Microfiber knot resonators (MKR) had a huge impact, not only in the field of sensing, but also in other fields such as, for example, ultrafast optics, due to its high Q-factor. In terms of sensing, a wide variety of parameters were able to be measured with this device: temperature [16]–[19], concentration of sodium chloride and refractive index [19]–[22], magnetic field [23], acoustic vibration [24], and humidity [25]. More recently, the aim of the researchers has been to incorporate new materials in the microfiber knot resonators in order to achieve new devices with enhanced sensitivity to the measured parameters [26]–[28]. In the same line of thought, this dissertation aims to combine devices such as fiber Bragg gratings (FBG) or Fabry-Perot (FP) interferometers in the microfiber knot resonators with the objective of obtain new sensors with improved sensitivity and possibly being able to discriminate between different physical parameters.

This dissertation is divided into 6 chapters. In this first chapter, the motivation for this work as well as the main goals that are to be accomplished with it are presented. It also includes the publications that resulted from this dissertation. Chapter 2 contains the state-of-the-art related to taper fabrication and to sensors that rely on taper configuration. It starts with an overview of the taper structure and its fabrication, giving special relevance to the CO_2 laser technique and the VYTRAN – glass processing workstation. Then, a brief overview of the sensors based on taper configuration is made. A deeper analysis with respect to the all-fiber interferometers using tapers and the microfiber knot resonators is performed.

Chapter 3 introduces a Mach-Zehnder sensor based on a large knot resonator. An explanation on how the sensor was produced is presented, followed by a description of the mode of operation of such sensor. A characterization of the sensor is performed in terms of refractive index and temperature. Finally, a comparison of sensitivities is made between this structure and the ones that were explored back in chapter 2.

Chapter 4 explores the concept of integrating devices into microfiber knot resonators in order to create new structures that can possibly act as sensors. In this chapter, two devices, a fiber Bragg grating and a Fabry-Perot (FP) cavity, were incorporated in microfiber knot resonators. First, the incorporation of a FBG in a MKR is demonstrated. A brief introduction about FBGs is presented, followed by a description of the fabrication and characterization of the sensor. Then, lastly, a FP cavity milled in a MKR using focused ion beam (FIB) milling is analyzed, starting out with a slight introduction about FP cavity and FIB technology. This chapter also includes a small

overview about the FIB composition, working principle and optical fiber preparation. A description about the fabrication process of this sensor is performed. Alternatives to this configuration are presented, as well as a preliminary refractive index characterization using one of the presented alternatives.

In chapter 5, a fiber Bragg grating in an abrupt tapered tip is studied. The fabrication and characterization in terms of refractive index and temperature are performed. Temperature independent refractive index sensing is explored using this sensor. Feasibility analysis is also performed on simultaneous measurement of refractive index and temperature.

At last, chapter 6 summarizes the whole thesis and presents some concluding remarks regarding the developed work. It also includes some guidelines and open issues that can potentially be carried out in the future.

1.2. Objectives

The main goal of this dissertation is to study new sensors based on tapers, namely knot resonators and interferometric sensors. Incorporating devices in microfiber knot resonators is also a goal that opens the possibility to create new and enhanced sensors. In such wise, the main objectives of this master's degree dissertation are the:

- Study of new sensing structures based on optical fiber tapers;
- Exploration of these new structures for sensing purposes;
- Study the incorporation of devices (FBG, FP) in microfiber knot resonators;
- Investigation of the viability of these new devices applied as sensors.

1.3. Scientific Publications

A. D. Gomes and O. Frazão, "Mach – Zehnder Based on Large Knot Fiber Resonator for Refractive Index Measurement," IEEE Photonics Technol. Lett., vol. 28, no. 12, pp. 1279–1281, Jun. 2016 [doi:10.1109/LPT.2016.2538963].

A. D. Gomes, B. Silveira, S. Warren-Smith, M. Becker, M. Rothhardt and O. Frazão, "Fiber Bragg Grating on Abrupt Tapered Tip for Temperature Independent Refractive Index Measurement", IEEE Sensors Journal, 2016 (Submitted).

1.4. Conferences

A. D. Gomes and O. Frazão, "Interferómetro de Mach-Zehnder baseado num Large Knot Fiber Resonator para sensorização de índice de refracção", In Física 2016 - 20ª

Conferência Nacional de Física, Braga, Portugal, September 8-10, 2016 (Accepted for Poster Presentation).

A. D. Gomes, B. Silveira, S. Warren-Smith, M. Becker, M. Rothhardt and O. Frazão, “Fiber Bragg Grating on Abrupt Tapered Tip for Refractive Index and Temperature Sensing”, In SEONs 2016 – XIII Symposium on Enabling Optical Networks and Sensors, University Beira Interior, Covilhã, Portugal, July 8, 2016.

Chapter 2
State of the Art

Tapers first appeared back in the end of the 20th century. They were initially used to fabricate single-mode fiber couplers [29]–[31]. Later on, as the years went by, new applications related to sensing started to emerge.

In this chapter, the taper structure and fabrication techniques are discussed. An analysis about sensors based on tapers is also made, as well as an overview of some of their configurations reported in literature.

2.1. Taper Structure and Fabrication Techniques

An optical fiber taper is performed by heating the fiber to its softening point while stretching it to decreasing its diameter in order to obtain a narrow stretched filament - taper waist - linked to the non-stretched fiber through a tapered section - taper transition. The taper transition can have different types of profiles: linear, parabolic, sinusoidal, polynomial or others [32]. To perform a particular profile, it is crucial to find a balance between parameters such as the heating source and the stretching.

The structure of an optical fiber taper is shown in Figure 2.1. It can be divided in three sections:

1. The down-taper - a transition zone where the fiber decreases its diameter with a specific profile, as shown before;
2. The taper waist - a narrow filament of fiber with uniform diameter, which is smaller than the initial fiber. This zone can be very small, long or it may not exist;
3. The up-taper - similarly to the down-taper, it is a transition zone where the fiber increases its diameter until it matches the original size.

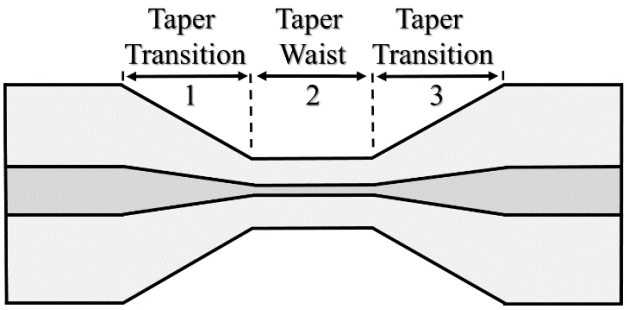

Figure 2.1. Structure of an optical fiber taper. 1: Down-taper; 2: Taper waist; 3: Up-taper.

There are different heating sources which are normally associated with the name of a specific taper production technique. It can be a flame [3], [33], where the flame moves under the optical fiber as it is being stretched, an electric arc [7], [34] created by two electrodes as in a splicing machine, or a focused CO_2 laser [35]. Next, the production methods using a focused CO_2 laser and using a VYTRAN - Glass Processing Workstation will be explored.

2.1.1 CO_2 Laser Technique

Conventional methods for taper fabrication, such as the flame fabrication, can contaminate the produced tapers with combustion by-products. Furthermore, other problems may arise from this techniques: non-uniformities in the waist diameter, hard control of the taper shape, among others [36]. Electric arc methods are also not so practical because of slow heat transfer from them to the fiber [35]. Therefore, in order to overcome this imperfections associated with the flame and the electric arc techniques, the fabrication of optical fiber tapers using a CO_2 laser began to be implemented.

Some theoretical studies about the production of tapers using a CO_2 laser have been performed back in the 90's [37], [38]. A precise control of the taper shape and waist radius was shown to be possible, in theoretical analysis, by using a point-like heat source that scans the fiber as it is being stretched [32]. For that, the CO_2 laser shows great advantages compared with other heating sources. Moreover, the CO_2 laser is clean, controllable, fast acting and free of inertia [35].

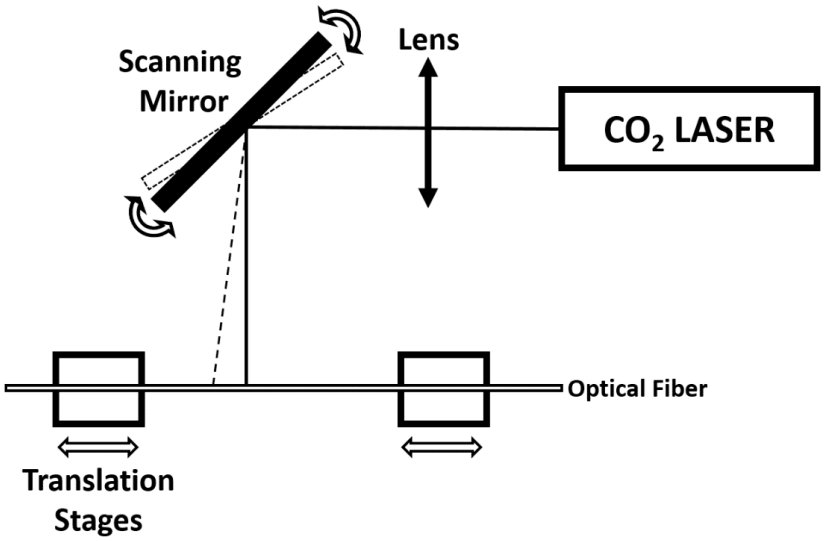

Figure 2.2. General scheme of the focused CO_2 laser technique configuration for taper production.

This technique uses a high-frequency pulsed laser emitting at a wavelength of 10.6 μm, which is strongly absorbed by silica fibers, inducing a long-term high

temperature. In comparison with continuous wave CO_2 lasers, high-frequency pulsed CO_2 lasers can generate high peak power providing a large stable temperature region in the optical fiber using quite low optical power [36].

A general scheme of the setup is presented in Figure 2.2. The configurations used by different authors, in literature, for this technique are very similar to each other [35], [36], [39], [40]. They all involve 4 major components:

1. A high-frequency pulsed CO_2 laser;
2. A lens to focus the beam with a desired spot size. Depending on the configuration it can be:
    a. a plano-convex lens, such as a ZnSe lens which has enough transmittance in the visible region, allowing the use of a visible beam, like a He-Ne laser, to perform alignments [35], [36], [40];
    b. a cylindrical lens, for focusing the beam along the vertical direction, perpendicular to the fiber, maintaining the beam shape in the direction parallel to the optical fiber [39];
3. A galvanometric scanning mirror to scan the beam across the optical fiber. This kind of mirrors are controlled by applying a voltage with a certain waveform profile. Bayle *et al*. [39] have studied the influence of this scanning waveform profile in the uniformity of the heating region along the optical fiber;
4. Two motorized translation stages used to stretch the optical fiber with resolutions that can go lower than 1 µm/step. These stages are normally controlled by computer.

Some authors use a He-Ne laser to coincide with the CO_2 laser in order to be used as a guide to direct the CO_2 laser beam onto the optical fiber [35].

Optical fiber tapers made using this technique can achieve diameters of a few micrometers at the taper waist. As an example, Ward *et al*. [40] produced tapers with 3 and 4 µm-diameter.

2.1.2 VYTRAN – Glass Processing Workstation

The VYTRAN - Glass Processing Workstation [41], [42] is a versatile glass processing platform capable of perform high-quality fusion splicing and tapering of specialty fibers. In Figure 2.3 are shown the constituents of the system: a filament-based heater that can heat optical fibers to temperatures up to 3000 ºC (see figure 2.4), precision stages (holding blocks) with multi-axis control to aid the alignment and positioning of the fibers for high quality splicing and tapering, a microscopic high resolution CCD imaging system and a personal computer.

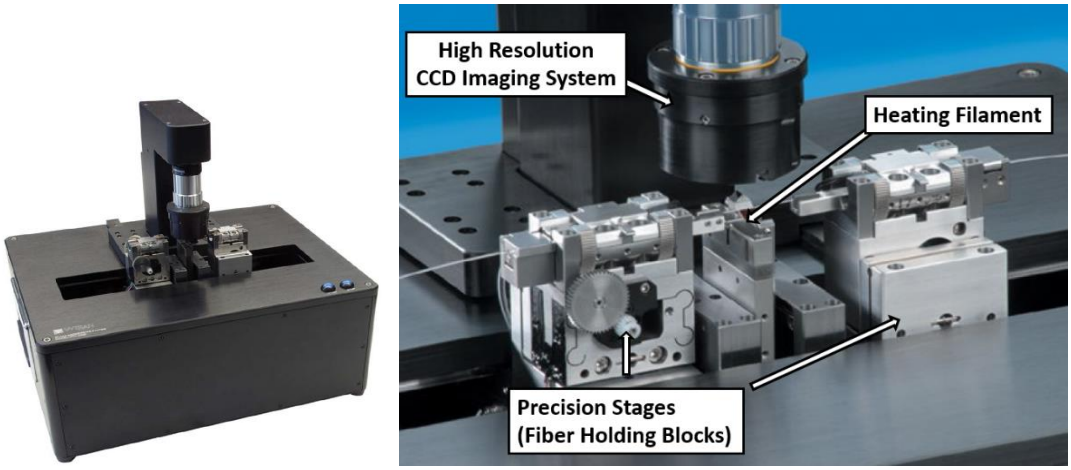

Figure 2.3. VYTRAN – Glass Processing Workstation [41], [42].

For drawing tapers, the optical fiber is heated to its softening point and a tensile force is applied to elongate the fiber, reducing its cross sectional area.

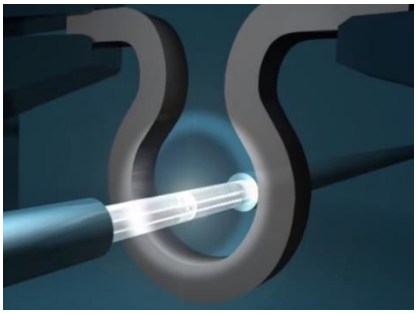

Figure 2.4. VYTRAN filament heater.

The mode of operation of the VYTRAN consists initially in stretching the fiber, tapering it down in order to create the down-taper (see section 2.1). When the fiber has been tapered down to a desired diameter, the workstation stops stretching the fiber and maintains a constant tension in order to obtain a constant desired diameter region (taper waist). Finally, to produce the up-taper region, the workstation diminishes the pulling force on the fiber until it is no longer stretching.

To fabricate tapers with the desired dimensions, other parameters should be adapted, such as the filament power, taper load positions, taper dimensions, pull velocity, and others, to achieve the perfect conditions.

2.2. Sensors based on Taper Configuration

Optical fiber tapers with micrometers (~1 µm - of the order of the wavelength of radiation propagation along the fiber) or even hundreds of nanometers diameter are usually called microfibers and nanofibers (MNF). In a microfiber, the fundamental mode is predominantly confined within the fiber. However, in nanofibers, where the diameter is much smaller than the propagated radiation wavelength, the fundamental mode is an evanescent mode which propagates mostly outside the nanofiber [43].

MNF proved to be very promising for sensing applications due to their strong confinement, large evanescent fields, great configurability (with the possibility to develop highly compact devices with complex geometries - 2D and 3D [5]) and low-loss connection [3]. They can also be used to create new miniaturized sensing platforms with fast response, higher sensitivity and low power consumption [1].

This type of sensors come in many different forms and normally the measured effects are sensed via intensity or phase change of the transmitted light. They can be divided in two major groups: the non-resonators and the resonators.

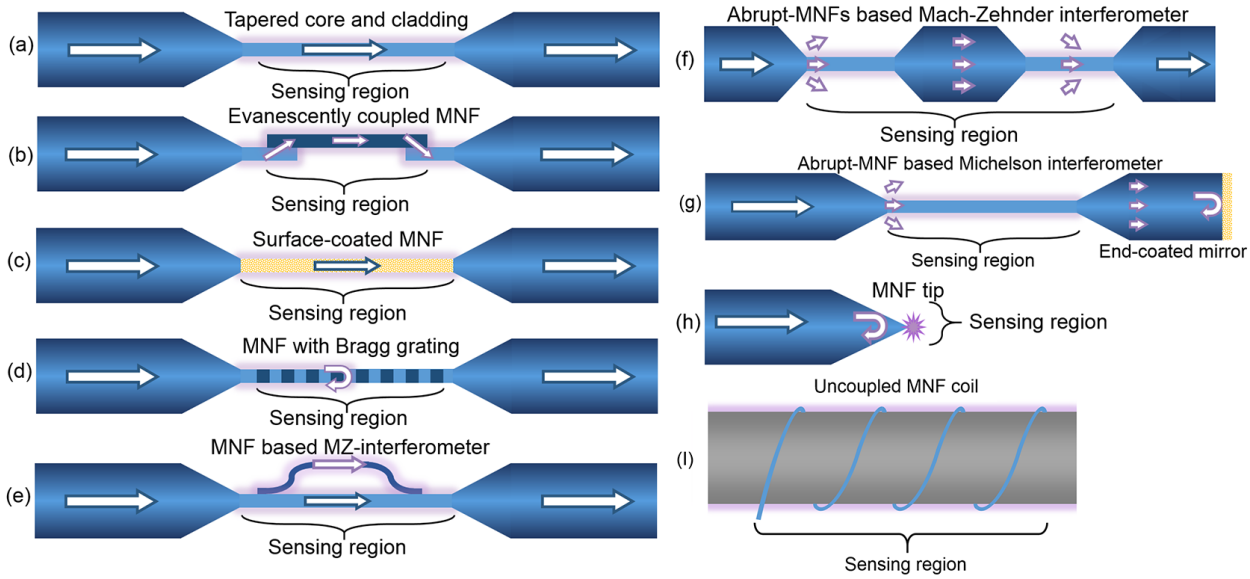

Figure 2.5. Illustration of common non-resonator-type MNF structures reported in literature. Adapted from Chen *et al.* [44]

In the literature, there are reported non-resonator MNF sensors with a wide variety of shapes for diverse applications, from physics to biology. The main attribute of these sensors is the ability to interact with the surrounding medium through the strong evanescent field of the guided mode(s).

Some non-resonator-type MNF structures reported in literature that can act as sensors are illustrated in Figure 2.5:

a. Straight MNF [45];
b. Straight MNF evanescently coupled to single-ended fiber [44];
c. Functionalization of the MNF surface to identify a specific chemical or biological component [6];
d. MNF with a fiber Bragg grating (FBG) [46] or a long period grating (LPG) [47];
e. Mach-Zehnder interferometer (MZI) made of two strands of MNF [48] or made of abrupt tapered sections [7];
f. Abrupt MNF Michelson interferometer [8];
g. MNF tip acting as a sensing head [49];
h. Uncoupled MNF coil [50].

Regarding the resonator-type MNF sensors, they involve all the sensors which use resonant structures. The mode of operation of these structures consists in tying a knot or coiling a MNF onto itself allowing coupling and evanescent overlap between modes propagating in adjacent turns, creating high quality factor optical resonators with a free spectral range (FSR) that depends on the length of the loop [3]. Moreover, their small-size and low fabrication cost have attracted much attention to produce them for sensing purposes [44].

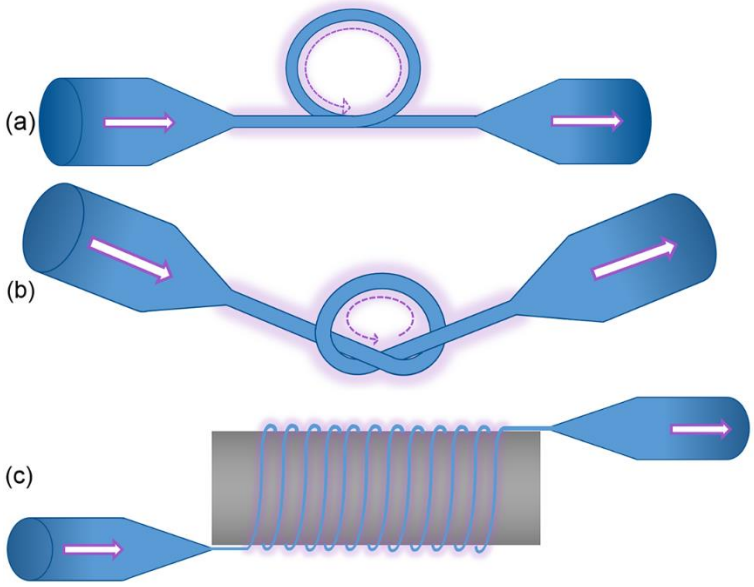

Figure 2.6. Illustration of resonator-type MNF structures. Adapted from Chen *et al.* [44]

This type of structures can be divided into three groups, as illustrated in Figure 2.6:

a. Microfiber loop resonator (MLR): it is a single turn (“loop”) of an optical microfiber taper in the taper waist region [5];
b. Microfiber knot resonator (MKR): it is made by tying a knot in an optical microfiber taper, creating a ring with micrometer dimensions [4];
c. Micro-coil resonator (MCR): it can be seen as a high-order MLR, which consists of several independent loop resonators. They present great potential ability of micro-assemblage in 3-D, for example, wrapping a microfiber onto optical rods [5], [43].

The following subsections will discuss more deeply two of these types of sensors: the all-fiber interferometers using tapers, from the non-resonator MNF structures, and the microfiber knot resonators, from the resonator-type MNF structures.

2.2.1 All-Fiber Taper Interferometers

Recently, optical refractive index sensors or refractometers based on all-fiber interferometers [7] or resonators [20] have been studied and developed due to their high sensitivity, broad measurement range and compact size [20]. From these all-fiber based interferometer sensors, the all-fiber Mach-Zehnder interferometer (MZI) has received considerable attention [7], [12], [51]–[53].

The MZI technique is used for measuring the refractive index (RI) of a media due to the phase shift of the guided light created by the media to be analyzed [11]. For refractive index and temperature sensing, many MZI configurations were studied and developed over the years. Michelson interferometer sensors can also be designed through an optical fiber taper [10].

Now, some configurations of all-fiber taper interferometers reported on the literature shall be explored with more detail.

Lu *et al.* [12] used a tapered fiber MZI, with 65 μm-diameter at the taper waist, for simultaneous measurement of refractive index and temperature. The sensor was created using simple fusion splicing of two single-mode fibers. A schematic of the sensor is shown in Figure 2.7. They achieved a sensitivity of -23.288 nm/RIU (refractive index units) for refractive index sensing and 61.5 pm/ºC for temperature sensing.

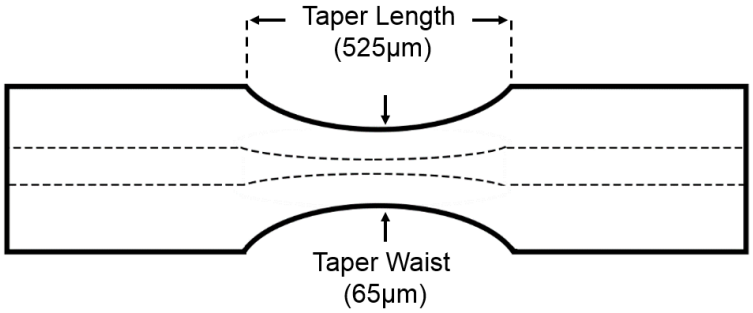

Figure 2.7. Schematic of the tapered fiber MZI. Adapted from Lu *et al.* [12]

Back in 2006, Kieu *et al.* [9] proposed a biconical fiber taper that was produced using the flame technique, achieving a waist diameter of around 8 µm. The mode of operation of this interferometer is based on the back and forth coupling of light between the single mode of the fiber and the two (or more) modes of the taper, where light propagates at the air-cladding interface of the taper waist. First, the fundamental mode propagating in the single-mode fiber is coupled into several modes of the taper in the down-taper. After traveling in the taper, the modes are coupled back into the single-mode fiber, in the up-taper region, interfering due to the phase difference between them. Sensitivities of ~650 nm/RIU and ~10 pm/ºC were obtained for refractive index and temperature measurements, respectively.

Using a simple optical fiber taper, a Michelson interferometer can also be built. For example, Amaral *et al.* [10] have developed an optical fiber inclinometer based on a fiber taper Michelson interferometer. The sensor, designed to work as a fiber-intermodal interferometer, consists in using an optical fiber taper, created using the electric arc technique, followed by a fiber tip-end, creating a mirror with 4% reflectance due to the Fresnel reflection on the glass-air interface.

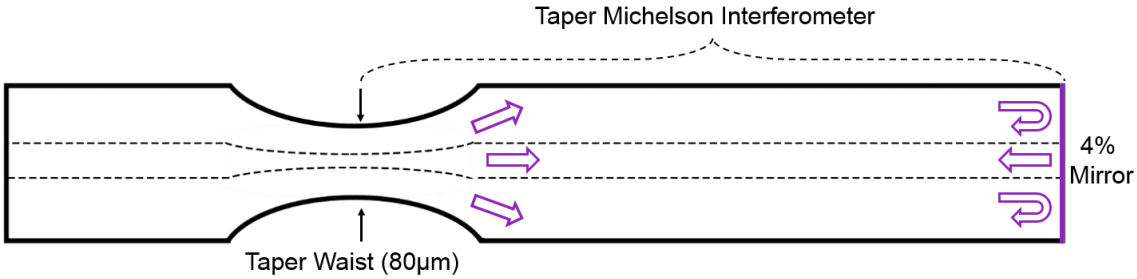

Figure 2.8. Schematic diagram of the fiber-taper Michelson interferometer. Adapted from Amaral *et al.* [10]

A schematic diagram of the sensor is presented in Figure 2.8. The demodulation of the interferometric phase signal is made by generating passively two quadrature phase-shift signals using two FBGs and following an interrogation configuration

demonstrated by Dahlem *et al* [54]. The interrogation configuration consists on analyzing the two phase-shifted signals using one photodiode for each wavelength. Because the two phase-shifted signals are in quadrature, the relative phase between them is π/2. The optical interference between the back-reflected core and cladding propagation modes occur at the taper region and a channeled spectrum is obtained [10]. The interferometric phase at one wavelength can be retrieved using the voltages of the photodiodes with a proper gain adjustment [54].

The curvature applied to the taper-tip cavity affects the coupling of the core modes to the cladding modes, changing the optical path distance between the core and the cladding modes, giving rise to a phase shift [10]. This phase shift can be analyzed as a function of the bending angle.

Going back to MZI configurations, one can have more than just one taper in the configuration. One of those cases is the single-mode fiber (SMF) based MZI presented by Tian *et al.* [7], which is a simple concatenation of two fiber tapers separated by a short (24-55 mm) middle section (Figure 2.9). For this sensor, a refractive index sensitivity of 17.1 nm/RIU was achieved.

One must note that, if the taper angle is large, part of the light couples from the core to the cladding and is attenuated by the coating. However, if within centimeters another similar taper structure is present, the cladding mode attenuation is negligible and the energy of this mode is coupled back into the core.

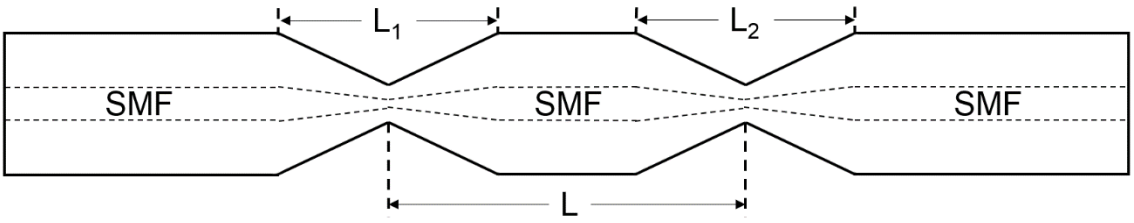

Figure 2.9. Structure of a two single-mode fiber tapers concatenated MZI. Adapted from Tian *et al.* [7]

The MZI in this sensor is created after the second taper, due to the phase difference caused by the different propagation constants of the core and cladding modes, which can be calculated using the following expression:

$$\phi = \frac{2\pi \Delta n_{eff} L}{\lambda} \quad (1)$$

where Δn_{eff} is the effective refractive index difference between the core and cladding modes, λ is the input vacuum wavelength and L is the length between the two tapers.

Δn_{eff} can be calculated using a broadband source and analyzing the attenuation maxima of the wavelength, which occur every $\phi = (2m + 1)\pi$. Hence, considering the separation of attenuation maxima wavelengths ($\Delta\lambda$), one can obtain:

$$\Delta n_{eff} \simeq \frac{\lambda^2}{L\Delta\lambda} \quad (2)$$

where λ is the peak wavelength and $\Delta\lambda$ is the separation between attenuation maxima wavelengths or, commonly known as FSR. With this, when a change in the effective refractive index occurs due to a change in the taper surrounding medium, a shift in wavelength is obtained:

$$\delta\lambda_m \approx 2\pi L\delta n_{eff} \quad (3)$$

where $\delta\lambda_m$ is the wavelength shift of an attenuation maximum and δn_{eff} is the change in the effective RI of the cladding mode, while the core mode effective RI stays almost constant. So, Δn_{eff} is changed by δn_{eff}. Note that if δn_{eff} is positive (an increase in the effective RI of the cladding mode is observed), Δn_{eff} decreases.

A refractive index sensor based on a MZI formed by three cascaded single-mode fiber tapers was presented back in 2011 by Wu *et al* [55]. In this structure, a weak taper is “sandwiched” between two tapers to improve the sensitivity of the device, obtaining a sensitivity of 28.6 nm/RIU for refractive index sensing, higher than the normal two cascaded taper based MZI that was explored before.

In 2012, an all-fiber in-line single mode-multimode-thinned single mode (SM-MM-TSM) MZI fiber structure was developed using only a splicing method. In this sensor, the thinned single mode fiber had a diameter of 80 μm. In terms of sensitivity, the sensor achieved −25.2935 nm/RIU for refractive index and 61.5 pm/ºC for temperature sensing [51].

A high resolution configuration is the MZI embedded in a thinned optical fiber, developed by Yang *et al* [56]. It consists in a long uniform flat fiber taper of a single-mode fiber (thinned fiber), made by flame technique, plus a pair of abrupt tapers made in the thinned fiber by electric arc-discharge using a conventional fusion splicer (Figure 2.10).

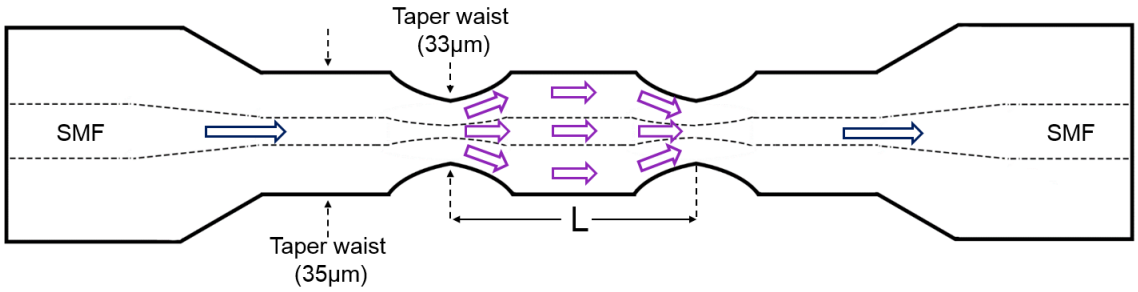

Figure 2.10. Schematic diagram of the MZI embedded in a thinned optical fiber. Adapted from Yang *et al.* [56]

The mode of operation of this sensor is based on the excitation of many cladding modes with different effective refractive indices at the first abrupt taper and the recouple of this modes back into the core, in the second abrupt taper, interfering with each other. The wavelength shift vs refractive index behavior is not linear, but in a short refractive index range (1.3997 to 1.4096), a high sensitivity of 2210.84 nm/RIU is obtained. Furthermore, the temperature sensitivity is -6.66 pm/ºC.

A comparison of sensitivities between all the different configurations presented in this subsection is summarized later in chapter 3, Table 3.2 for refractive index and table 3.3 for temperature sensing.

2.2.2 Microfiber Knot Resonators

Another type of sensors that have received a lot of attention in the past few years were the micro-resonators. To this class of devices belong the microfiber knot resonators, as one saw previously in section 2.2. The way to produce a MKR is by tying a knot in an optical microfiber taper, creating a ring with micrometer dimensions [4]. The taper in the knotted zone allows the evanescent field of light to couple between adjacent sections of the taper, creating therefore resonance [57]. This overlap of the fiber with itself allows no need for a precise alignment [4]. Most of these sensors detect the measuring parameter (refractive index, temperature or others) by analyzing the wavelength shift as a function of the parameter.

The sensing applications of microfiber knot resonators are huge, namely temperature sensing [16]–[19], concentration of NaCl and refractive index sensing [19]–[22], magnetic field sensing [23], acoustic sensing [24], humidity sensing [25], among others.

A more detailed analysis of some published results will now be made regarding some MKR configuration for refractive index and temperature sensing.

In 2009, Wu *et al.* [18] reported a simple silica MKR, with around 190 µm-diameter, assembled using a 1.7 µm-diameter microfiber. For this sensor a Q-factor of around 12000 was obtained. When used for temperature sensing, the sensor could achieve a sensitivity of 52 pm/ºC from 30 ºC up to 700 ºC.

Later on, and also for temperature sensing, Yang *et al.* [17] used a simple MKR for seawater temperature sensing. A Q-factor of $3.0x10^4$ and a maximum sensitivity of 22.81 pm/ºC were reported for a MKR with 473 µm-diameter, made of a 3.91 µm-diameter microfiber.

One should take into account that silica and seawater have opposite thermal response due to their opposite thermal-optical coefficient. The evanescent field and the influence of the negative thermo-optic coefficient of seawater become weaker when the fiber diameter increases. As the authors reported, 2.5 to 4 µm-diameter microfibers have higher sensitivity. Thereby, it is important to have an equilibrium between the thermo-optic coefficient and the fiber diameter to maximize the results.

A comparison between silica MKR, and a polymer MKR was also presented by Wu *et al* [18]. The polymer MKR reported has 98 µm-diameter, assembled from a 2.1 µm-diameter polymer microfiber. A Q-factor of around 8000 and a sensitivity of -266 pm/ºC were obtained. In this case, the polymer MKR presented a lower Q-factor but a much higher temperature sensitivity than the simple silica MKR. In fact, the thermal expansion coefficient and the thermal-optical coefficient of polymer microfibers are larger than those of silica. Hence, the temperature sensitivity of polymer MKRs is higher. However, the range of temperatures is much reduced (from 20 ºC to 80 ºC), compared with the silica MKR, which can handle temperatures almost 10 times higher.

Also in temperature sensing field, Zeng *et al.* [16] presented a 55 µm-diameter MKR, assembled by two fiber probes in a glass substrate, all coated with a low-index polymer as shown in Figure 2.11. Two sensitivities were obtained: 270 pm/ºC in the heating process, from 28 ºC to 140 ºC, and -280 pm/ºC in the cooling process, from 135 ºC to 25 ºC.

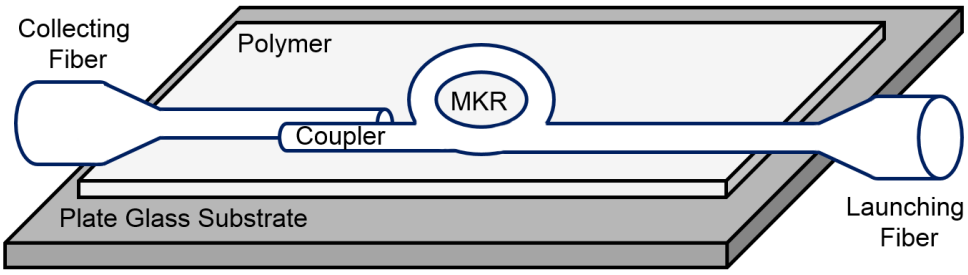

Figure 2.11. Schematic of a MKR temperature sensor with two single-mode fibers used as a launching and collecting fiber. Adapted from Zeng *et al.* [16]

More recently, Yu *et al*. [22] reported a polymer MKR made of a 1.3 µm-diameter microfiber for refractive index sensing, achieving a sensitivity of about 95.5 nm/RIU in the RI range from 1.39 to 1.41. A detection limit of about 2.1×10^{-5} was also obtained.

Still for refractive index sensing, Lim *et al.* [19] proposed a MKR with around 0.5 mm-diameter in a Sagnac loop reflector. The microfiber structure was embedded in low refractive index Teflon, except the MKR sensing region, to obtain a balance between responsiveness and robustness. A schematic of the experimental setup is depicted in Figure 2.12. For this sensor, a sensitivity of 30.49 nm/RIU was obtained. The temperature response was also analyzed, showing a sensitivity of 20.6 pm/ºC.

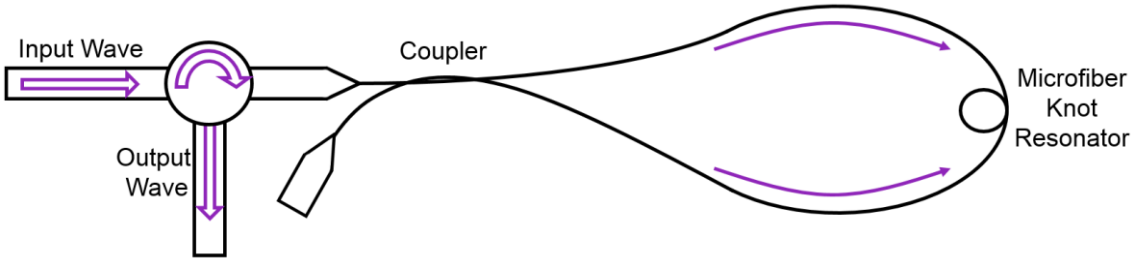

Figure 2.12. Schematic diagram of a MKR in a Sagnac loop. Adapted from Lim *et al.* [19]

Back in 2014, Li *et al.* [20] developed a MKR coated with Teflon for refractive index sensing. For applying the polymer, a dip-coating technique was used, which process is outlined in Figure 2.13. The MKR initial diameter was 1.02 mm but, after coated, it was reduced to around 0.45 mm. The microfiber initial diameter was 2.92 µm, increasing to 3.95 µm after the Teflon coating, whose estimated thickness is of around 0.5 µm. A sensitivity of approximately 31 nm/RIU was reported for this sensor.

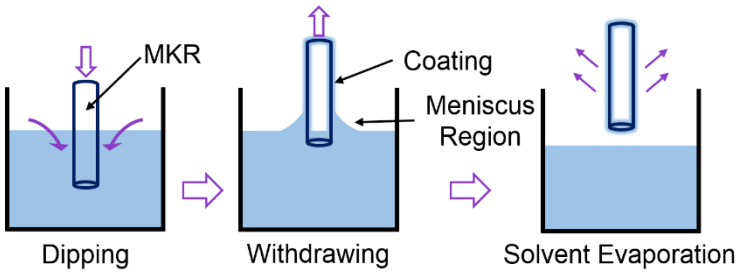

Figure 2.13. Illustration of the dip-coating process in Teflon. Adapted from Li *et al.* [20]

Another factor explored by Li *et al.* [20] was the optical degradation of the MKR over time. In fact, the transmission losses of a bare MKR increased at the speed of around 0.24 dB/h[1], reaching 18 dB after 3 days, unlike the coated MKR where no change was noticed for half a month. This result shows that Teflon coating, using the proposed method, provides protection to the MKR against degradation over time.

In the last year, Xu *et al.* [21] created an interesting small-size refractometer for detecting slight refractive index variations based on cascaded microfiber knot resonators (CMKR) with Vernier effect.

The Vernier effect is commonly used in calipers and barometers to enhance the measurement accuracy through the overlap between lines on two scales with different periods. In this case, the setup uses two MKR with millimeters of diameter (1.178 mm and 1.230 mm) assembled from a microfiber of 1.9 µm-diameter. An illustration of the used configuration is presented in Figure 2.14.

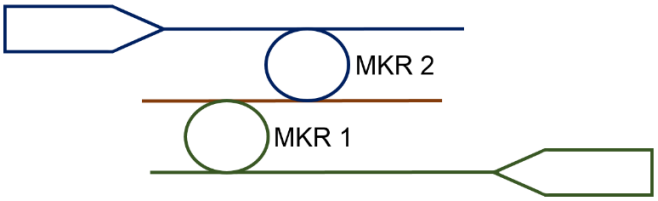

Figure 2.14. Illustration of the MKR in a cascaded configuration. Adapted from Xu *et al.* [21]

In the experiment, the ambient RI of the first MKR is kept constant (1.3315), while the ambient RI of the second MKR is slightly varying. The wavelength shift due to the RI change was measured and a sensitivity of 6523 nm/RIU was obtained. This sensor allows a resolution of 1.533×10^{-7} RIU because the measured wavelength shift is an absolute parameter dependent on the relative optical intensity variation. So, relative

[1] dB/h - dB per hour

intensity noise in the light source, thermal noise and shot noise in the photo-detector of the spectrum analyzer do not affect the RI detection. Furthermore, if the first MKR is embedded in a low RI polymer, such as Teflon, it increases its robustness and long-term stability, ensuring the first MKR to be immune to ambient RI changes.

Again, a comparison of sensitivities between all the different MKR configurations presented in this subsection is summarized later in chapter 3, Table 3.2 for refractive index and Table 3.3 for temperature sensing.

Chapter 3
Mach-Zehnder based on Large Knot Fiber Resonator

Optical fiber tapers have proven to be very useful, especially as sensors because of their outstanding mechanical properties and large evanescent fields [1], [3]. A wide variety of physical, chemical and biological sensors based on optical fiber tapers have been demonstrated over the years [1], [44].

In terms of sensing, optical fiber tapers were first studied as refractometers, due to the interaction of their large evanescent field with the surrounding medium [58]. Then, diverse sensing applications, such as bending, pressure, strain and temperature, were demonstrated [9], [13], [59]. As previously explored in chapter 2, many configurations using optical fiber tapers were developed for diverse applications, of which the all-fiber interferometers and the microfiber resonators are examples [4], [7].

This chapter presents a Mach-Zehnder based on a large knot fiber resonator (MZ-LKR) with a diameter of a few millimeters used for refractive index sensing of liquids. The knot is made on a taper with around 60 µm-diameter fabricated with the CO_2 laser technique, as explored in chapter 2.1.1.

3.1. Fabrication and Characterization

The sensor was made manually by tying a knot in a tapered single mode optical fiber (SMF28) creating a ring. The taper was fabricated at INESC TEC using a CO_2 laser technique to reduce the fiber diameter to ~60 µm. The used CO_2 laser setup is similar to the one described in chapter 2.1.1. It consists of a 30 watts CO_2 laser source, 2 mirrors to elevate the beam, a plano-convex lens with a 100 mm-focal length to focus the beam on the optical fiber, 2 Aerotech motorized stages to stretch the optical fiber, a concave mirror with a 150 mm-focal length to refocus the beam on the other side of the fiber, and a camera to observe the tapering process. A picture of the setup is presented in Figure 3.1 and the parameters used to produce the taper are displayed in Table 3.1.

After tying the knot, the diameter of the ring was then reduced until it reaches a value of ~3.5 mm. The knot is located near the transition zone between the untapered SMF and the tapered section.

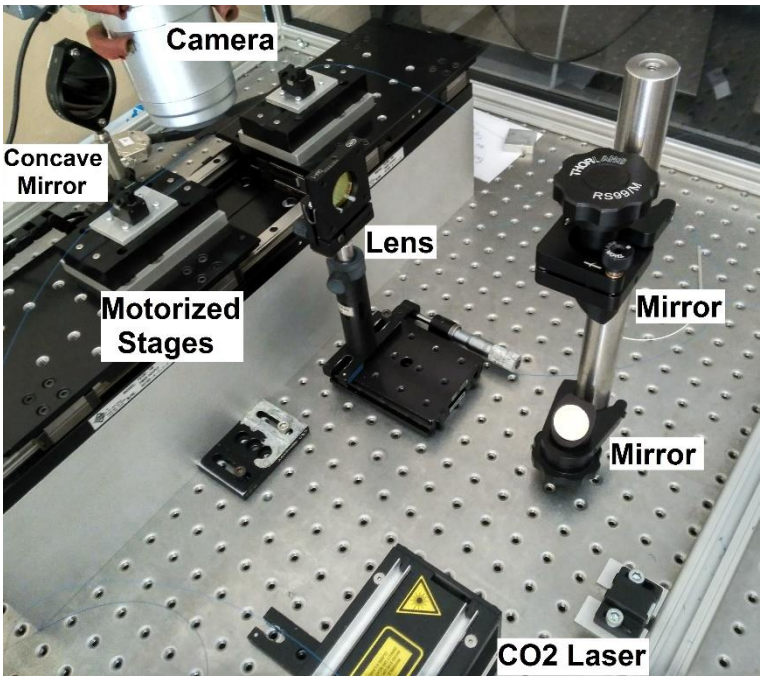

Figure 3.1. Picture of the CO2 laser setup.

CO_2 laser power	3 W
Leading stage speed	600 µm/s
Back stage speed	130 µm/s

Table 3.1. Parameters used for producing the taper.

Figure 3.2a shows the experimental setup. It consists in a broadband source with a central wavelength of 1550 nm and a bandwidth of 100 nm connected to an optical fiber where the MK-LKR is located. The transmitted signal spectrum is observed in an optical spectrum analyzer (OSA) with 1 nm resolution. The sensor is immersed in liquid. This allows it to be studied under different liquids with different refractive indices. The setup also allows a gradual heating of the liquid.

In Figure 3.2b, a 1 cm-diameter MZ-LKR in air is shown, illuminated by a He-Ne laser. The MZ-LKR interferometer is formed by the two contact points in the knot, visible in Figure 3.2c.

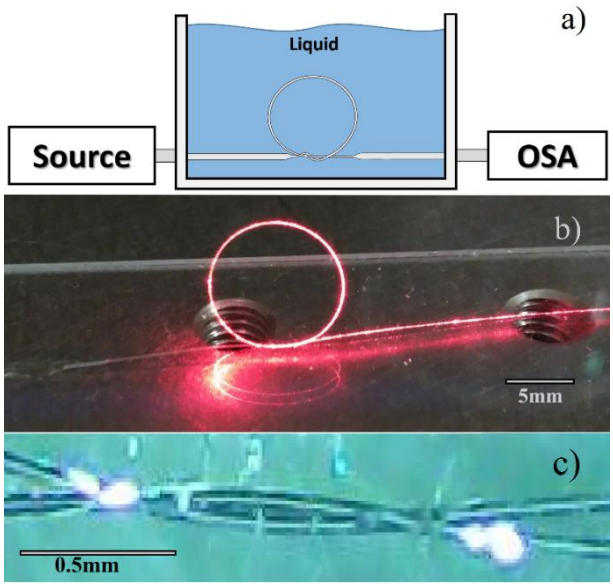

Figure 3.2. a) Experimental setup. b) MZ-LKR in air, illuminated by a He-Ne laser. c) Photograph of a knot of a MZ-LKR with 3.5mm diameter.

The transmitted signal spectrum of a 3.5 mm-diameter MZ-LKR, in air and in liquid (ethylene glycol, n=1.426), illuminated by a broadband source can be observed in figure 3.3.

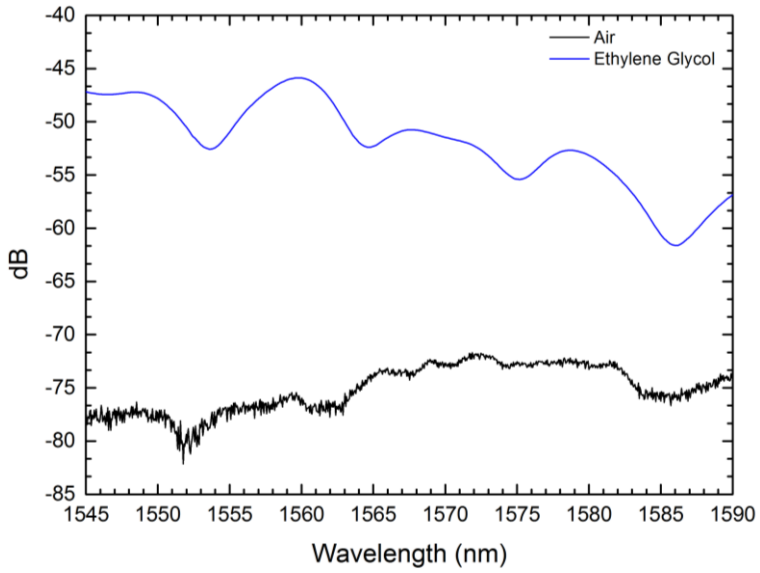

Figure 3.3. Transmitted signal of the MZ-LKR when it is in air and when it is immersed in ethylene glycol (n=1.428). The free spectral range (FSR) in ethylene glycol is approximately 10.15 nm.

The mode of operation of the MZ-LKR is the following: in air, light travels in the ring and is lost in the loop and in the knot due to curvature losses (see Figure 3.2b). Around the two contact points in the knot (Figure 3.2c), the presence of air does not allow light to be coupled between adjacent sections because of the high confinement of light due

to the large taper diameter. Hence, the light cannot pass directly to the output of the ring and a low power signal is observed. When the sensor is immersed in liquid, the light in the contact points of the knot is now less confined and capable of coupling between adjacent fibers, with a certain phase difference, giving rise to an interference spectrum. This interference is visible in Figure 3.3. Part of the light is now capable of passing directly to the output of the ring, without losing itself in the loop, and a spectral signal with higher intensity is observed in the OSA.

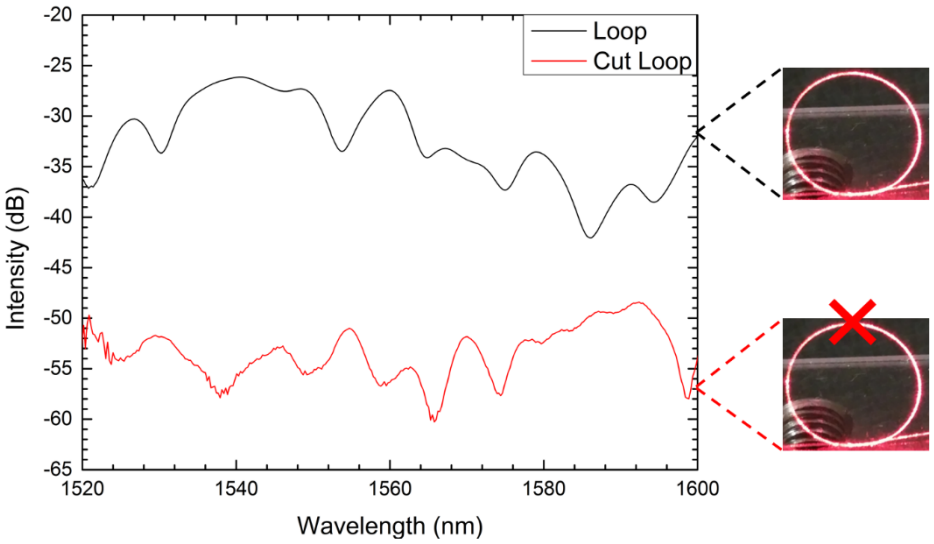

Figure 3.4. Transmitted signal of a MZ-LKR immersed in ethylene glycol (n=1.428) before and after cutting the loop, while fixing the knot structure.

In order to demonstrate this behavior, a MZ-MKR was immersed in ethylene glycol (n=1.428) and, while fixing the knot region, the ring was cut. The transmitted signal of the sensor before and after the cut is depicted in Figure 3.4. After cutting the loop, the interference pattern is still present in the transmission spectrum, although it is slightly changed due to a shape modification in the contact region of the knot structure, even fixing the knot shape as much as possible. A reduction in the intensity is observed because the ring is cut and the measured light in the OSA comes from the coupling in the knot region (Figure 3.2c). However, the loop is very important to maintain the shape of the knot region and to increase the detected power.

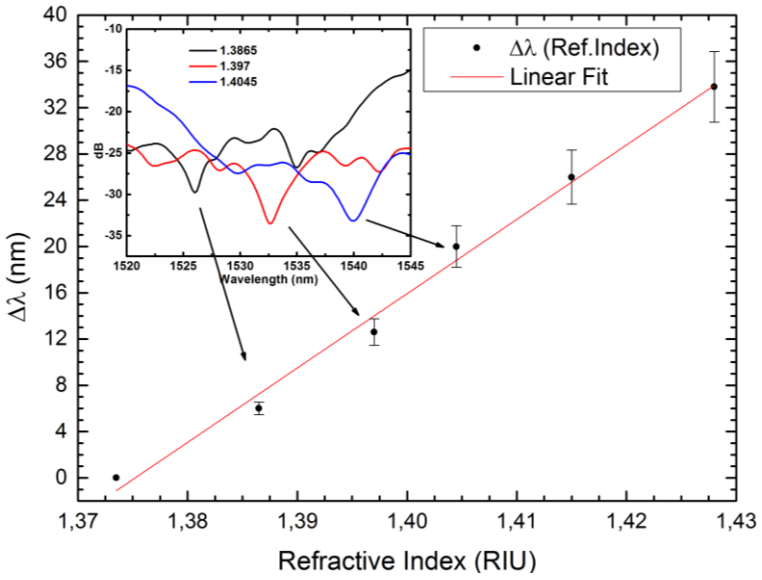

Figure 3.5. Wavelength shift as function of refractive index. The inner plot shows the spectra of the transmitted signal for three different refractive index.

The peak shift of the transmitted signal spectrum from the sensor was studied by dipping the sensor in ethylene glycol mixtures with different refractive indices [60], from 1.3735 to 1.4280. The refractive index of the different ethylene glycol mixtures was measured before the experiment using an Abbe refractometer. The wavelength shift as function of the refractive index is presented in figure 3.5. As the wavelength shift is directly proportional to the refractive index [11], a linear fit was applied. From this fit, a sensitivity of 642 ± 29 nm/RIU was obtained. The auxiliary graph in Figure 3.5 clearly shows the wavelength shift due to refractive index change.

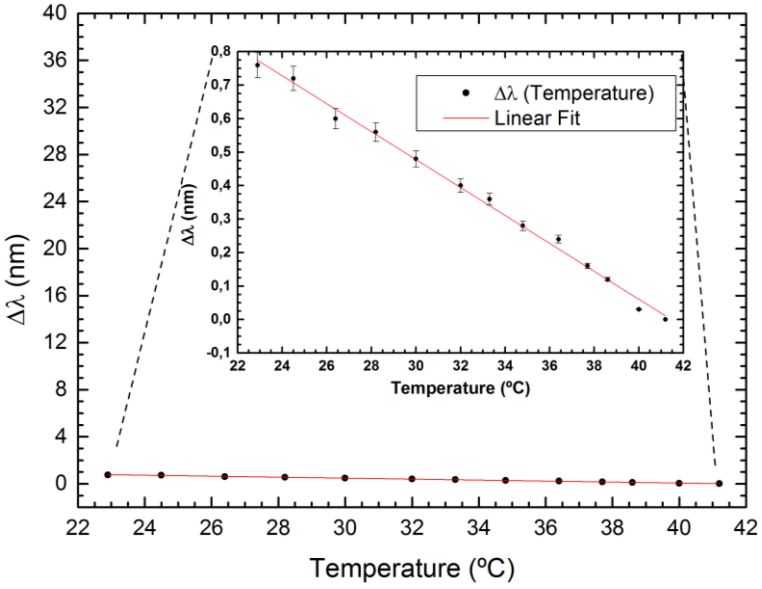

Figure 3.6. Wavelength shift as a function of temperature.

The study of the wavelength shift of the sensor as a function of temperature variations was also performed. The MZ-LKR was immersed in water whose temperature was progressively increased from 22.9 to 41.2ºC. The wavelength shift as a function of temperature is depicted in Figure 3.6. A linear fit was performed on the data and, from this fit, a sensitivity of -42 ± 9 pm/ºC was obtained. The negative sensitivity is related to the knot dimension, being the thermo-optical effect dominant in this case. Dividing both sensitivities, a value of 6.5×10^{-5} RIU/ºC is reached, showing a low influence of temperature in the refractive index measurement.

Author	Type	RI Sensitivity	RI Range
This work	**Large Knot Resonator**	**642 nm/RIU**	**1.3735 – 1.4280**
[7]	SMF based MZI	17.1 nm/RIU	N/A
[12]	Tapered Fiber MZI	-23.188 nm/RIU	N/A
[51]	SM-MM-TSM MZI	-25.2935 nm/RIU	1.3345 – 1.3775
[55]	MZI of 3 cascaded tapers	28.6 nm/RIU	N/A
[19]	MKR in Sagnac loop	30.49 nm/RIU	1.334 – 1.348
[20]	MKR coated with teflon	~31 nm/RIU	1.3322 – 1.3412
[22]	Polymer MKR	95.5 nm/RIU	1.39 – 1.41
[9]	Biconical fiber taper	~650 nm/RIU	1.333 - 1.350
[56]	MZI embedded in a taper	2210.84 nm/RIU	1.3997 – 1.4096
[21]	Cascaded MKR	6523 nm/RIU	1.3320 -1.3350

Table 3.2. Comparison of sensitivity between different configurations for refractive index sensing.

Author	Type	Temp. Sensitivity	Temp. Range
This work	**Large Knot Resonator**	**-42 pm/ºC**	**22.9 – 41.2ºC**
[56]	MZI embedded in a taper	-6.66 pm/ºC	39 – 70ºC
[9]	Biconical fiber taper	~10 pm/ºC	N/A
[19]	MKR in Sagnac loop	20.6 pm/ºC	30 – 130ºC
[17]	Simple MKR for seawater	22.81 pm/ºC	N/A
[18]	Simple silica MKR	52 pm/ºC	30 – 700ºC
[51]	SM-MM-TSM MZI	61.5 pm/ºC	20 – 80ºC
[12]	Tapered fiber MZI	71 pm/ºC	20 – 60ºC
[18]	Simple polymer MKR	-266 pm/ºC	20 – 80ºC
[16]	MKR coated with polymer	270 pm/ºC (Heat.)	28 – 140ºC
[16]	MKR coated with polymer	-280 pm/ºC (Cool.)	135 – 25ºC

Table 3.3. Comparison of sensitivity between different configurations for temperature sensing.

3.2. Discussion

The refractive index sensing of liquids was achieved with a MZ-LKR. For refractive index sensing, a sensitivity of 642 ± 29 nm/RIU was obtained in a refractive index range from 1.3735 to 1.4280 with a resolution of 0.009 RIU. For temperature sensing, a sensitivity of -42 pm/ºC was observed. Comparing the sensitivity with previous published results and with other different configurations, as shown in Table 3.2 and in Table 3.3, the MZ-LKR stands in a zone where most of the remaining configurations have less sensitivity, except the MZI embedded in a taper [56] and the cascaded MZI configuration [21]. The refractive index sensitivity of the sensor is similar to the biconical fiber taper [9]. However, in terms of temperature both sensors have different sensitivities, but they are of the same order of magnitude as the already published MKR and MZI, except for the polymer MKR [18] which reveals a significant increase in the sensitivity due to the polymer. Moreover, the sensor presents a wider refractive index range and works with refractive indices closer to silica, a region where the other configurations cannot reach. The sensor showed a cross sensitivity of 6.5×10^{-5} RIU/ºC. The principle of working of this device was also explored. The size of the MZ-LKR allows it to be easily made and manageable. The sensor is more resistant due to its dimensions, revealing an advantage in relation to the micrometer size knot resonators.

Further studies should be performed to investigate the influence of the number of contact points in the knot in the signal spectrum, as well as to determine if there is any predominance of one contact point over the other in the interference spectrum.

Chapter 4

Microfiber Knot Resonator with Devices

4.1. Fiber Bragg Grating embedded in a Microfiber Knot Resonator

A fiber Bragg grating (FBG) is a periodic modulation of the refractive index along the optical fiber. The modulation is created by exposing the fiber core to an intense optical interference pattern, for example, using an ultraviolet femtosecond laser [61], [62]. When light propagates through the modulated refractive index region, it will partially reflect at each interface of higher and lower refractive index. For a specific wavelength all the partial reflections will add up in phase, reflecting the incident light to values that can go nearly to 100%. For the other wavelengths, the reflections are out of phase, cancelling each other, which result in high transmission [63].

Fiber Bragg gratings are one of the most essential fiber sensing elements. They have been designed and developed for a wide variety of sensing applications: strain [64], temperature [65], pressure [66], bending [67], among others.

In this section, the incorporation of a fiber Bragg grating in a microfiber knot resonator (MKR) is demonstrated. This new device opens the possibility to explore simultaneous measurement of different parameters by monitoring the spectral response of the FBG and the MKR.

4.1.1 Fabrication and Characterization

The proposed structure is depicted in Figure 4.1. It consists of a taper with an FBG inscribed in the taper waist region. Then, this taper is used to create a MKR, being the FBG inside the MKR structure.

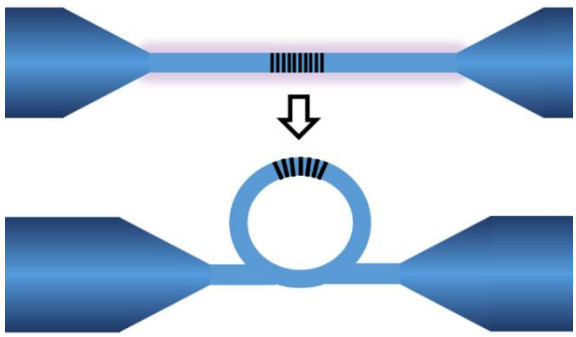

Figure 4.1. Schematic of the sensor. This structure is assembled from an FBG inscribed in a taper.

But first, before inscribing the grating, one should know the spectral response of a MKR structure. To do so, a taper was fabricated using the VYTRAN machine, as explored back in section 2.1.2, with the following characteristics:

Down-Taper length	10 mm
Up-Taper length	17 mm
Taper waist diameter	13 µm
Taper waist length	12 mm
Filament Power	52 W

Table 4.1. Characteristics of the VYTRAN produced taper.

Note that the obtained taper waist diameter was 9 µm, which is smaller than expected (13 µm). This also happens for the up-taper length.

A MKR was produced by tying a knot on the taper, creating a 1.24 mm-diameter ring. The transmission spectrum of the structure was measured using a broadband source with a central wavelength of 1550 nm and a bandwidth of 100 nm, and an optical spectrum analyzer (OSA) with 0.02 nm resolution. The result is depicted in Figure 4.2.

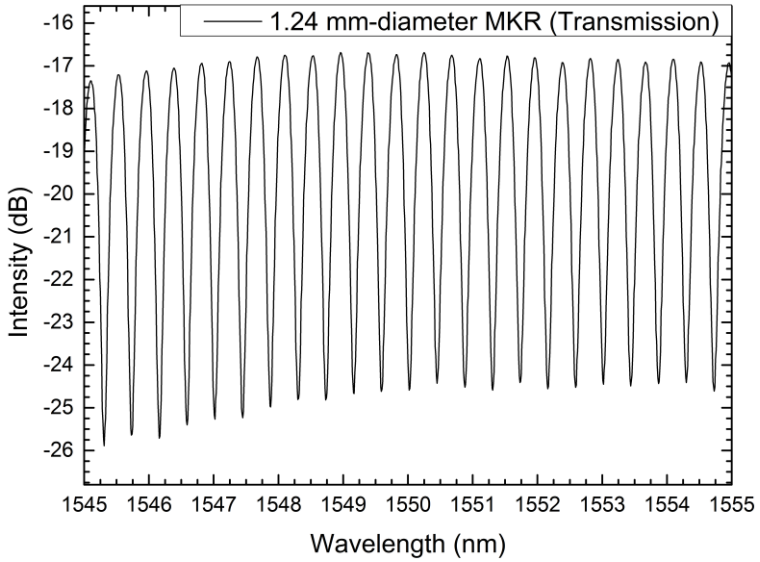

Figure 4.2. Transmission spectrum of a 1.24 mm-diameter MKR.

The transmission spectrum is an interference pattern with resonant peaks. As explored back in chapter 2, the free spectral range (FSR) of the MKR, which is the distance between two resonant peaks, depends on the length of the ring.

The FSR of a cavity is given by [68]:

$$FSR \approx \frac{\lambda^2}{n_{eff} L} \qquad (4)$$

where n_{eff} is the effective refractive index of the taper and *L* is the cavity length. In this case, the cavity length is the perimeter of the ring, which is given by $2\pi r$. From Figure 4.2, the FSR at 1550 nm is 430 pm. Using these values in equation (4) and considering 1.4384[2] for the effective refractive index of a 9 µm-diameter taper, one can calculate the ring diameter. For such values, the calculated ring diameter is 1.236 mm, which is close to the value measured with a caliper (1.24 mm).

To observe the spectrum of the FBG in the MKR, it is necessary to measure the final structure in reflection. Hence, it is convenient to know the spectrum of the MKR in reflection. For this purpose, one end of the MKR was spliced to a silver coated fiber tip that reflects the light back to the MKR. The other end of the MKR was connected to an optical circulator to observe the reflected signal in the OSA. The spectrum of the MKR in reflection has the same interference pattern as in transmission, however the power is decreased by 3 dB.

The FBG was inscribed in a taper, with the same characteristics as the one used before, using a phase-mask interferometer (Talbot interferometer) driven by an ultraviolet femtosecond laser (267 nm) [69], [70]. An illustration of the Bragg grating inscription setup is depicted in Figure 4.3.

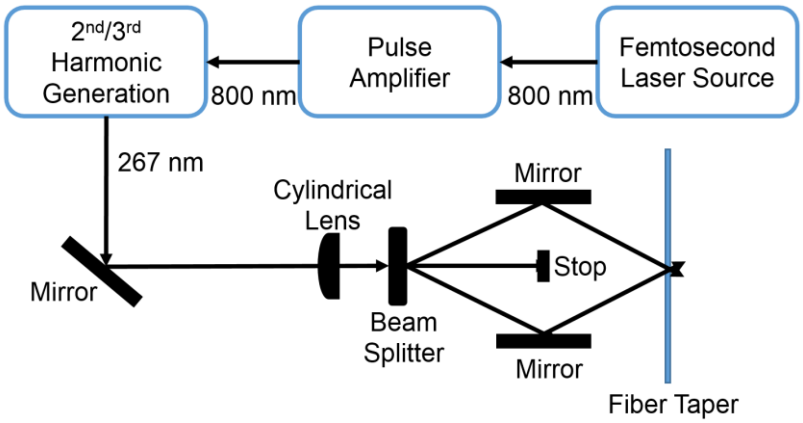

Figure 4.3. Bragg grating inscription setup using two-beam interference with UV femtosecond laser pulses. Adapted from Becker *et al.* [69], [70]

The interferometer consists of a cylindrical lens, to focus the beam in the direction perpendicular to the fiber, a beam splitter which is a diffraction grating with a period of 1075 nm, diffracting the beam, and 2 mirrors to guide the first order diffraction modes

[2] See Appendix B.1

into the fiber taper. The interference of these 2 beams in the fiber taper will create a Bragg grating with a period which is half of the mask period (537.5 nm), if the 2 mirrors are correctly aligned.

The taper presents a waist diameter of approximately 9 µm which is mainly composed of pure silica (n=1.444 @1550 nm). So, a long inscription time of 10 minutes was used with a laser power of 250 mW.

The FBG was measured in reflection using an optical circulator and a broadband source with a central wavelength of 1550 nm and a bandwidth of 100 nm connected to the optical circulator. The reflection spectrum was observed in an OSA with 0.02 nm resolution and is presented in Figure 4.4.

The Bragg wavelength is given by:

$$\lambda_B = 2n_{eff}\Lambda \qquad (5)$$

where n_{eff} is the effective refractive index of the considered mode and Λ is the period of the Bragg grating. Since the Bragg grating period is 537.5 nm and the fundamental mode reflection peak is centered at 1545 nm, the effective refractive index of the fundamental mode should be 1.437.

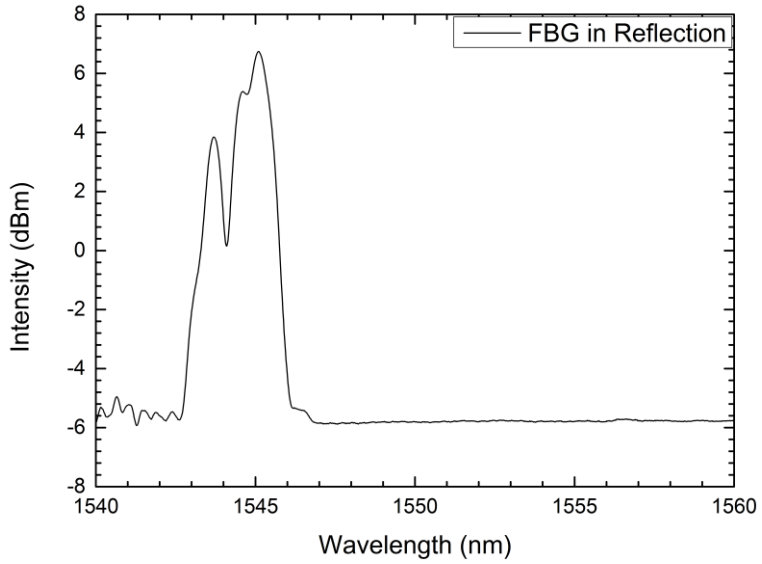

Figure 4.4. Reflection spectrum of the FBG inscribed in a 9 µm-diameter taper.

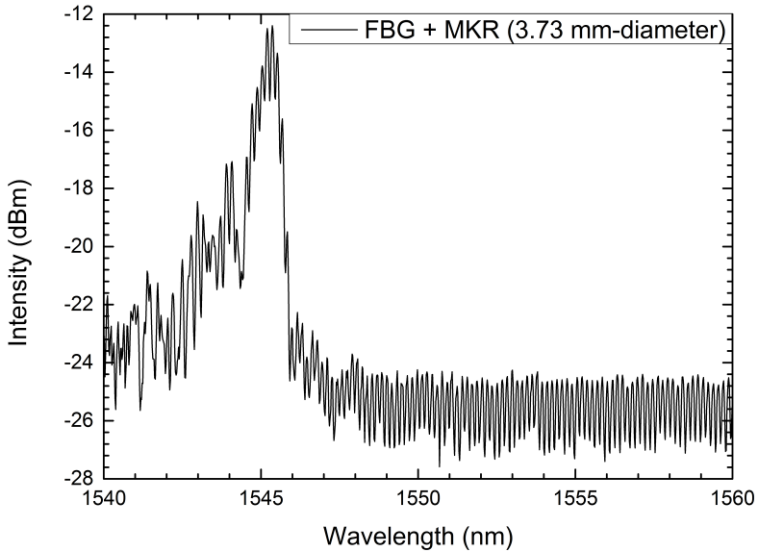

Figure 4.5. Reflection spectrum of the FBG embedded in a 3.73 mm-diameter MKR structure.

A MKR with 3.73 mm-diameter was created using this taper, with the FBG inside the MKR structure. The reflection spectrum of the structure is shown in Figure 4.5. The interference behavior of the MKR spectrum is now modulated by the previous FBG spectrum. It is visible that the FBG spectrum is maintained, however with a huge decrease in intensity due to curvature losses or to light coupling to the outside of the fiber by the grating.

4.1.2 Discussion

An FBG embedded in a 3.73 mm-diameter MKR structure was demonstrated. The FBG was inscribed in a taper using a phase-mask interferometer driven by a femtosecond laser. The inscribed FBG has a period of 537.5 nm, which corresponds to a Bragg wavelength of 1545 nm for the fundamental mode of this taper.

The spectrum of a MKR was studied in transmission and in reflection. The diameter of the MKR was estimated using a relation involving the FSR and the effective refractive index of the MKR. The estimated value matches the measured one. The MKR spectrum in reflection has proved to be the same as the transmission spectrum, except with an intensity decrease of 3 dB.

The resulting reflection spectrum of the final sensing structure (FBG and MKR) is a combination of the FBG reflection spectrum with the MKR spectrum. The structure opens the possibility to explore the implementation of this sensor for simultaneous measurement of different parameters, for example temperature and refractive index. If the FBG reflection peak and the MKR interference pattern are characterized in refractive index and temperature, it should be possible to measure both parameters at the same

time. This can be done by monitoring the wavelength shift of both, the FBG reflection peak and the MKR interference peaks, and use a matrix method to obtain the refractive index and temperature variations independently.

Moreover, this sensor can also be explored in terms of curvature. Since the FBG is inside the MKR structure, it suffers strain/curvature that will induce a variation in the effective refractive index and in the grating period that can lead to a change in the Bragg wavelength or even originate chirp.

4.2. Fabry-Perot Cavity embedded in a Microfiber Knot Resonator using Focused Ion Beam Milling

Optical fiber Fabry-Perot (FP) cavities have been extensively studied for sensing a variety of physical parameters with high sensitivity and accuracy, such as strain [71], pressure [72], temperature [73], and others [74], [75]. Furthermore, a FP cavity can as well be used to measure the refractive index of a fluid when exposed to it [76]. This measurement is performed by monitoring the phase shift of the cavity's interference signal.

More recently, fiber-integrated FP resonators became especially attractive for the reason that they present a linear response with high sensitivity and large dynamic ranges [76], [77]. Fiber-integrated FP resonators are produced by digging an air slot, reaching the core of the fiber. Thus, there is the formation of standing waves inside the air cavity. Apart from having high sensitivities, FP resonators also present very low cross-sensitivity (of the order of 5×10^{-6}) [78], [79].

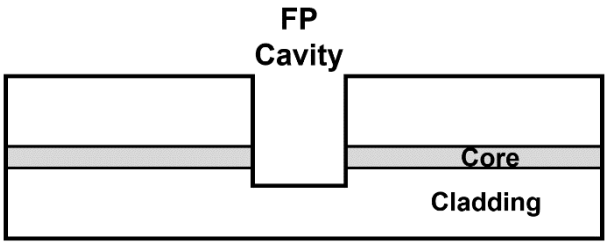

Figure 4.6. Schematic of a FP interferometer cavity in a single mode fiber.

Not a long time ago, FP interferometers (Figure 4.6) fabricated in single mode fiber (SMF) started to be made using micromachining with a femtosecond laser [79], [80]. Despite being a versatile tool for micromachining, femtosecond lasers have limits in terms of achieving machined surfaces with good quality and smoothness. The rough surfaces created with this technique originate strong light scattering, leading to poor mirror reflectivity. A FP with poor mirror reflectivity results in an interference pattern with low fringe visibility [77]. In order to overcome this problem a chemical etching process may be used to remove sputtered remains adhering to the surface of the cavity or, alternatively, a short laser wavelength must be used to obtain better surface roughness [76]. Note that the spatial accuracy is limited by diffraction, but in this case it is not very important unless the realized features have sub-wavelength dimension size.

An alternative to femtosecond lasers is the use of focused ion beam (FIB) milling. Micromachining with FIB allows milling with detailed profiles and better surface finishing than femtosecond laser micromachining due to its thin and controllable spot size (a few

tens of nanometers) [77]. There is no need for additional etching processes using this milling tool [76].

FIB milling has been used for diverse optical fiber applications: long period gratings (LPG) [81], [82], nano-FBGs [83] micromachining of fiber tips, milling of side access holes on structured optical fibers [84], direct core structuring of microstructured optical fibers [85], and FP microcavities [86]–[88].

In this section, the fabrication of a FP cavity in a microfiber knot resonator (MKR) is performed using FIB milling. The device is produced with the objective of achieving simultaneous measurement of refractive index and temperature by monitoring the joint response of the FP and the MKR, compacting both structures into a single sensor.

4.2.1 Focused Ion Beam Milling and Sample Preparation

The working principle of the FIB milling consists in transferring energy from the accelerated ions to chemically bonded atoms by collision. This process transfers enough energy to exceed the atom-atom binding energy plus the material work function, causing ejection of the material - what is called sputtering. One small problem regarding this process is the redeposition of a fraction of the ejected atoms on the open milled region, which makes the amount of removed material hard to control [84].

For a given material, the milling rate depends on the ion species and energy, as well as on the angle of incidence of the beam and the surrounding atmosphere [89].

A schematic diagram of the FIB constituents is depicted in Figure 4.7. The FIB structure is similar to a scanning electron microscope but, in this case, it works with gallium ions and not with electrons. First, the ions are generated at the ion source and extracted by applying an electric field. Then, the beam is refined at the spray aperture and condensed in the first lens. The stigmatism of the beam can be corrected at the upper octopole.

The variable aperture is used to vary the beam current, normally between 1 pA and 10 nA, with an ion beam energy between 10 and 50 keV. This mechanism allows the system to have both, a fine beam which can be used for high-resolution imaging on sensitive samples, and a heavy beam used for fast and rough milling [90].

The suppression of the beam can be executed using the blanking deflector and aperture. The beam can be scanned along the sample, with a desired pattern, using the lower octopole. In the second lens the beam is focused in a fine spot, with a best resolution achievable of sub-10 nm. The multichannel plate (MCP) is used for imaging by collecting secondary particles that result from the process.

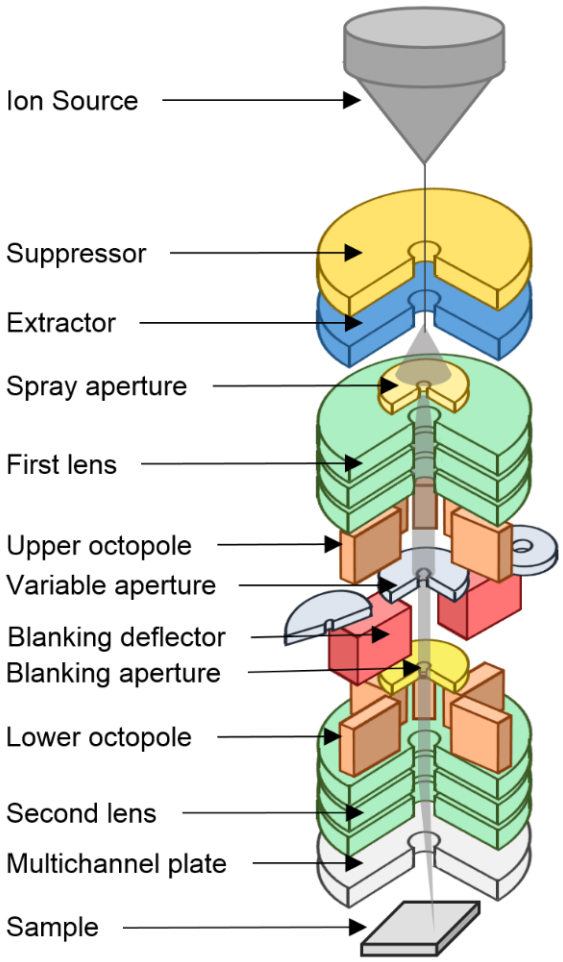

Figure 4.7. Schematic diagram of a focused ion beam ion column. Adapted from Reyntjens *et al.* [90]

The FIB system used in this work operates with gallium ions (Ga^+), which have positive charge. The Ga^+ ions accelerated into the sample promote the emission of backscattered and sputtered ions along with secondary electrons with different rates. The net injection of positive Ga^+ is only partially compensated by these ejected electrons, leading to an excess of charge building on the surface of the sample which will cause random deflections of the incident beam [84].

One way to solve the problem is to cover the sample with a conducting material in order to dissipate the electric charge in excess. In this experiment, the sample was fixed on an aluminum holder using a conductive silver paste. Then, a thin film of tantalum was sputtered in the whole set. Other materials such as platinum could be used, but they are more expensive than tantalum. To perform the deposition of the tantalum thin film, a sputtering chamber was used.

4.2.2 Fabrication and Characterization

A microfiber knot resonator (MKR) was made using a 60 mm-long taper with 27 µm-diameter in the waist region. The taper was fabricated using the same CO_2 laser technique as in chapter 3. The transition regions of this taper are very abrupt, inducing an interference pattern in the spectrum due to light couple into cladding modes in the down-taper and recouple back in the up-taper. The structure of this interference pattern remains slightly after performing the microfiber knot resonator, as shown in Figure 4.8. The created MKR has a diameter of around 4.5 mm.

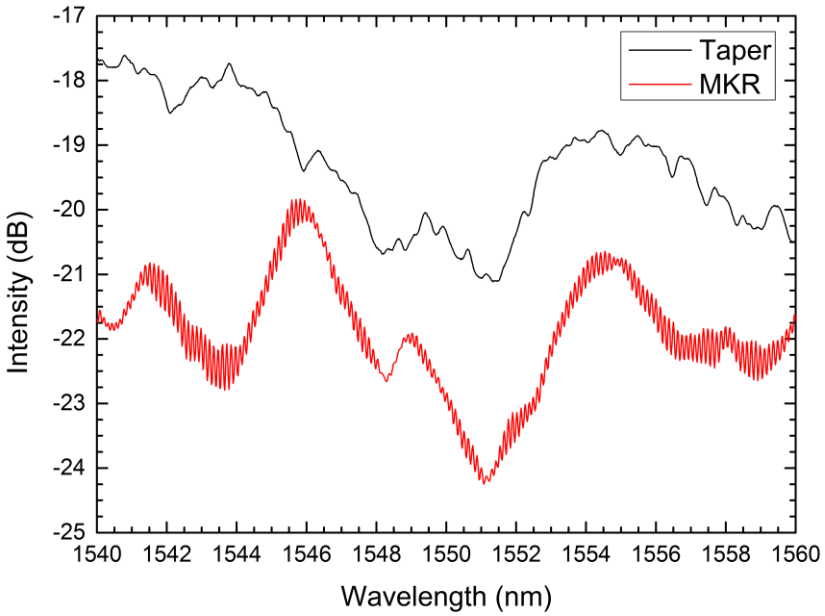

Figure 4.8. Taper spectrum before and after the microfiber knot resonator creation.

The MKR was mounted on an aluminum holder, glued with a conductive silver paint in the SMF zone to create an electrical contact between the fiber and the holder. Then, a thin film of tantalum was sputtered in the whole set.

The deposition of the tantalum thin film was executed in a small sputtering chamber. The sample was placed 5 cm bellow the tantalum target. The injection of argon in the vacuum chamber was regulated in order to obtain a pressure of around 8×10^{-3} mbar. The sputtering was performed with a current of 60 mA during 100 seconds, which corresponds to a film thickness of around 50nm. These values were previously optimized by some colleagues at the IPHT.

A scanning electron microscope (SEM) image of the MKR before the milling is presented in Figure 4.9a. The image scale is incorrect since it was taken in wide view mode and not in resolution mode. In wide view mode it is impossible to focus the object and the MKR was too wide to be observed completely in resolution mode.

To create the cavity in the MKR structure, a Tescan (Lyra XMU) FIB-SEM (focused ion beam – scanning electron microscope) was used. The gallium beam comes tilted by 55º from the vertical axis. Hence, the sample was tilted 55º relative to the same axis so that the aluminum holder surface is perpendicular to the gallium beam.

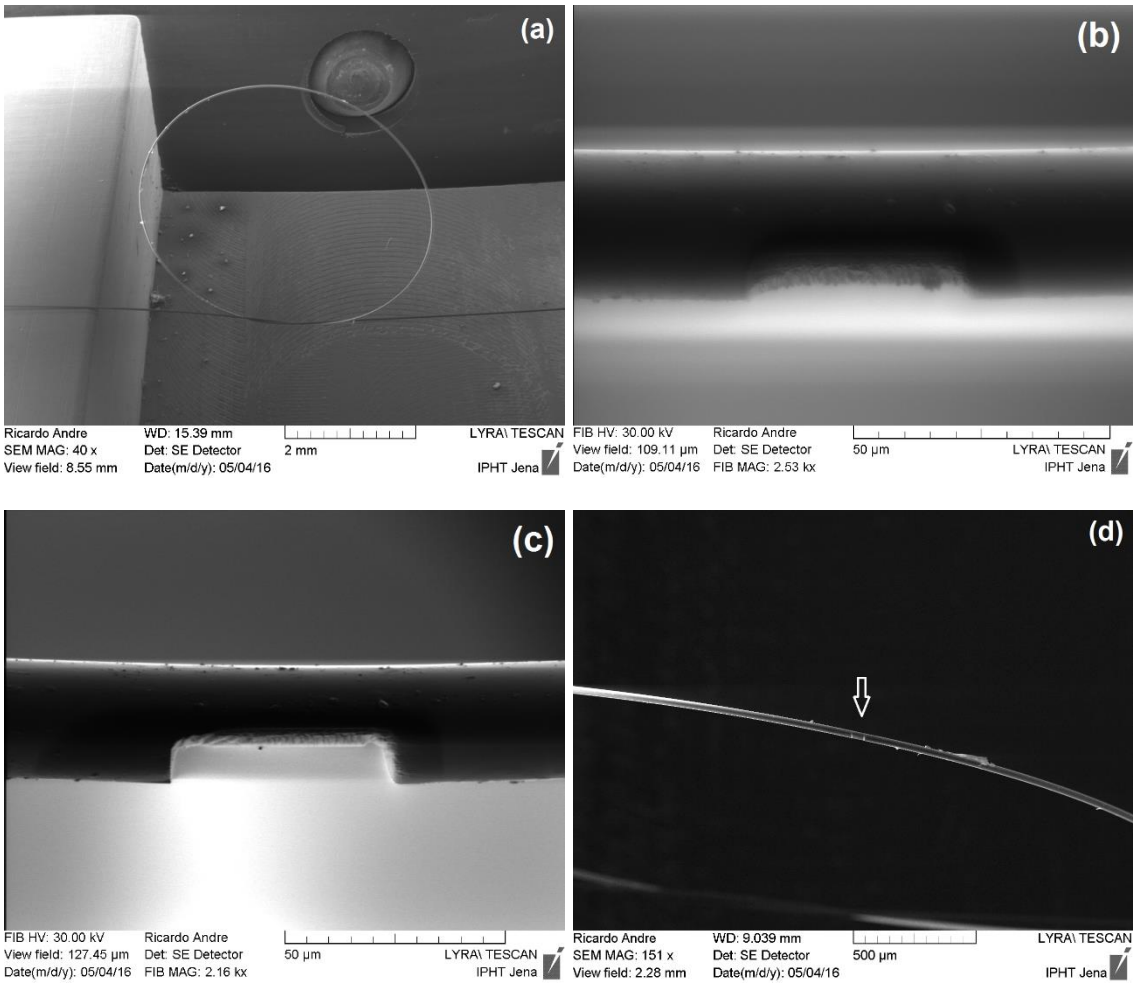

Figure 4.9. (a) Scanning electron microscope (SEM) image of the MKR before milling. Note that the scale is incorrect because the picture was taken in wide view mode and not in resolution mode. (b) Focused ion beam (FIB) image of the Fabry-Perot cavity after some minutes of milling. (c) FIB image of the final cavity. (d) SEM image of the Fabry-Perot cavity location in the MKR structure.

A cavity with 8 µm height, 40 µm wide and 20 µm deep was milled on the top of the MKR with a current of 2.1 nA. Then, the surfaces of the Fabry-Perot cavity were polished using a current of 1000 pA. A FIB image of the milled cavity during and after the milling process is shown in Figure 4.9b and c. A SEM image of the cavity location in the MKR structure is presented in figure 4.9d.

From the way the sensor was mounted on the holder, the MKR was suspended in the air and it was likely to move. These factors have contributed to a shift of the ring when hit by the gallium beam during the milling process, being necessary to make

constant adjustments in the position of the milling area. Moreover, to perform a good polishing of the cavity surfaces in order to reflect the light beam, it is necessary that the structure does not move during the polishing process. Given this scenario, the cavity surfaces were not well polished due to a movement of the structure, creating irregular surfaces. These rough surfaces induce light scattering, introducing losses in the system. Regarding this, a noisy spectrum is expected in the transmission spectrum. The transmission spectrum of the structure, before and after the sample preparation and milling process, is depicted in Figure 4.10.

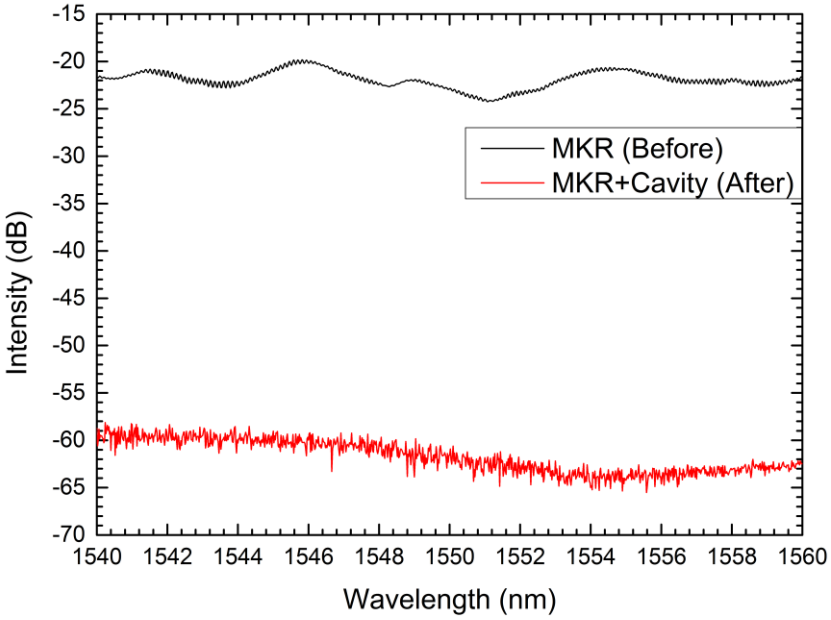

Figure 4.10. Transmission spectrum of the MKR before and after the sample preparation and milling process.

First, it is important to figure out what is the origin of the losses: if the losses are due to the tantalum coating, an alternative needs to be found in order to minimize it; if they arise from the cavity, a better way to polish the cavity surfaces may solve the problem.

To study the losses induced by the tantalum coating, a new MKR was made with a diameter of around 4.2 mm, using a taper with the same characteristics as the one used before. The sensor mounted in the aluminum holder and a tantalum coating was sputtered in the whole structure. Figure 4.11 represents the transmission spectrum of the MKR before and after the tantalum coating. The huge losses created by the tantalum coating bring the MKR spectrum to noise level.

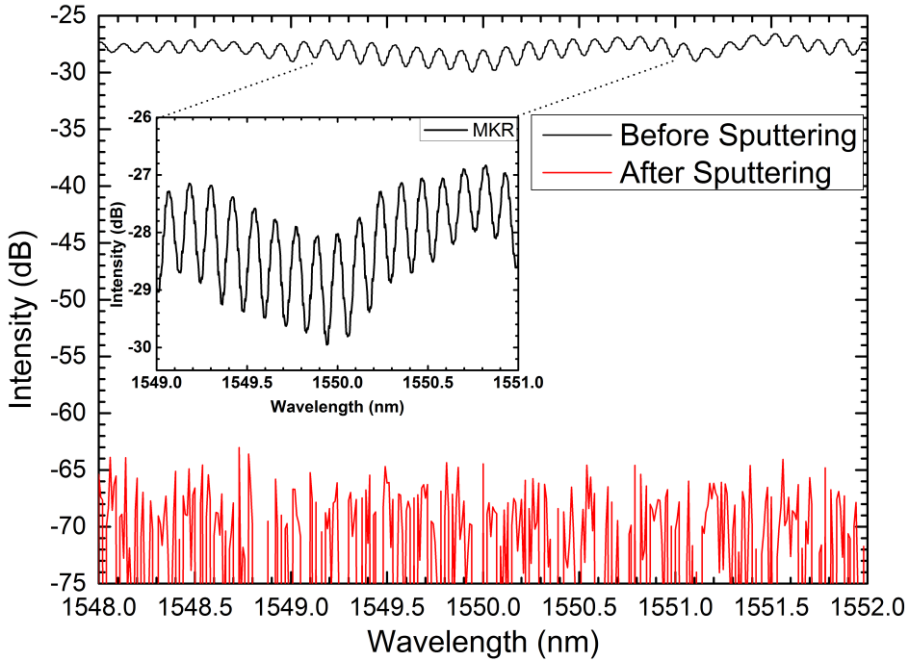

Figure 4.11. Transmission spectrum of the MKR before and after the tantalum sputtering. The inset shows a zoom of the MKR spectrum before sputtering.

Therefore, to overcome this and other problems some actions must be taken:

- Reduce the coated area, especially in the transition regions of the taper, to reduce the losses induced by the tantalum coating;
- Remove as much as possible the tantalum coating using the focused ion beam;
- Fix the MKR structure to avoid movement during the milling process for a good surface polishing.

A MKR with a diameter of around 1.6 mm was created from a taper with the same characteristics as the ones used before. The sensor was mounted in an aluminum holder with the ring structure parallel to the surface of the holder, lying on it. The whole structure was covered with delicate task wipers to avoid tantalum sputtering in these areas, except in a small part of the MKR where the cavity is to be created. In this uncovered region, the MKR was glue to the holding block using silver paint to make an electric contact avoiding charge effects. This time, the silver paint will induce some losses since it is now located in the taper and not in the SMF zone. Then, a tantalum coating was sputtered in the structure. The parameters used for the sputtering were the same as the ones used before: sample 5 cm away from the tantalum target, a current of around 60 mA with a sputtering time of 100 seconds and a chamber pressure of around 8×10^{-3} mbar.

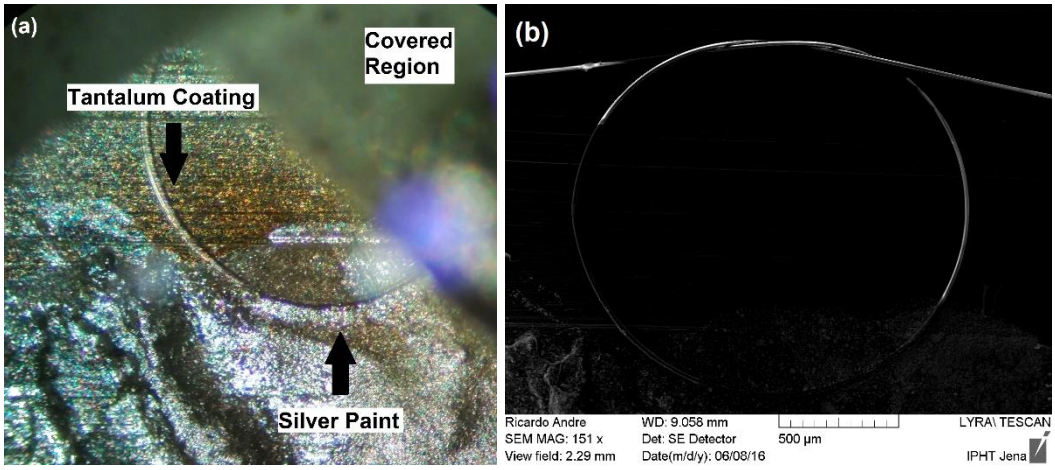

Figure 4.12. (a) Picture of the MKR mounted on the aluminum holder. (b) SEM image of the MKR after removing the covered region.

A picture of the MKR after the sputtering is presented in Figure 4.12a. The cover was removed and the structure was placed in the SEM/FIB system. A SEM image of the MKR is shown in Figure 4.12b. The darkest part of the fiber is a region covered by the tantalum film and the uncoated region of the fiber is brighter due to charge effects.

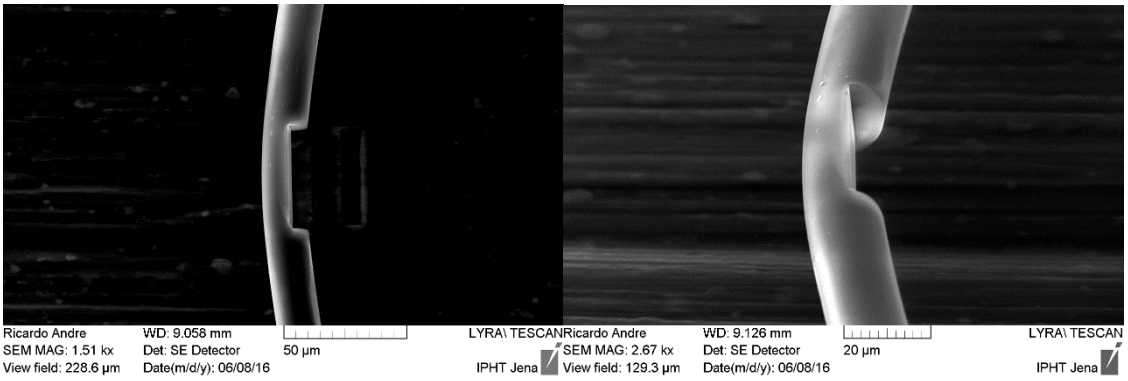

Figure 4.13. SEM images of the Fabry-Perot cavity in the MKR.

An 8.8 µm height, 40 µm wide and 15 µm deep Fabry-Perot cavity was created in the coated region on the top of the MKR. First, the cavity was milled with a current of 850 pA during more than 2 hours. This low current value will create a smoother cavity and remove less coating in the surroundings, which is good for polishing the surfaces afterwards. The bottom of the cavity was polished using the same current, with a depth of 15 µm, during 24 minutes. Then, the cavity surfaces were polished with a current of 650 pA during 6 minutes. A SEM image of this cavity is shown in Figure 4.13. In the end, the tantalum coating was removed using the FIB.

To remove the silver paint, a droplet of acetone was used. However, this droplet was enough to break the MKR in the cavity position, showing how fragile this kind of

structures can be. Regarding this, one can think of new alternative configurations to this problem. Two possible alternatives are depicted in Figure 4.14.

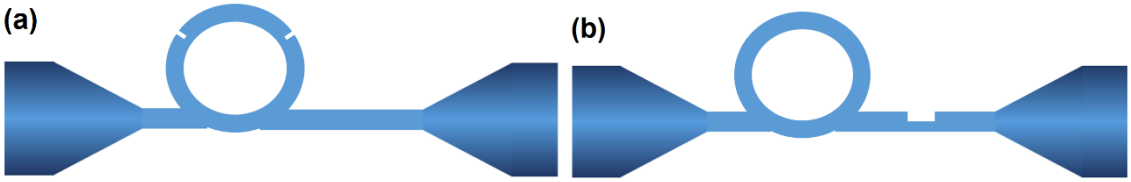

Figure 4.14. Alternative configurations: (a) 2 small rips in the MKR structure creating a silica cavity; (b) a cavity in the taper region next to the MKR structure.

The first idea is to create 2 small rips in the MKR structure that will work as mirrors of the silica cavity created between them (Figure 4.14a). Despite inserting weak points in the MKR structure, the amount of milling required is reduced. To avoid introducing fragile points in the MKR structure, a Fabry-Perot cavity can be milled in the taper region next to the MKR structure, as shown in Figure 4.14b. In this configuration, the MKR structure stays intact. Considering that the probability of breaking is higher in the first case, the second idea was chosen.

To create a sensor using the model shown in Figure 4.14b, a MKR was made using an 11 µm-diameter taper. This taper was produced using the VYTRAN machine (see section 2.1.2), with the same characteristics as the one used in section 4.1.1.

A SEM image of the MKR is presented in Figure 4.15a. The ring has a diameter of around 700 µm. A droplet of silver paint was used to glue the taper region right next to the MKR structure into the holder, creating an electric contact. The fiber was also fixed to the holder in the SMF region next to the taper with the same silver paint. The whole structure was covered except in the taper region between the silver contacts. A tantalum film was sputtered with the same parameters as used before. In the end, only the right half of Figure 4.14b is covered with the tantalum film.

A 45 µm wide, 5 µm height and 15 µm deep Fabry-Perot cavity was milled using a current of 1000 pA after the silver paint contact right next to the MKR. The 3 sides of the cavity were polished using the same current. The final cavity length obtained was 47.8 µm (Figure 4.15b and c). In the end, the tantalum coating was removed using the FIB.

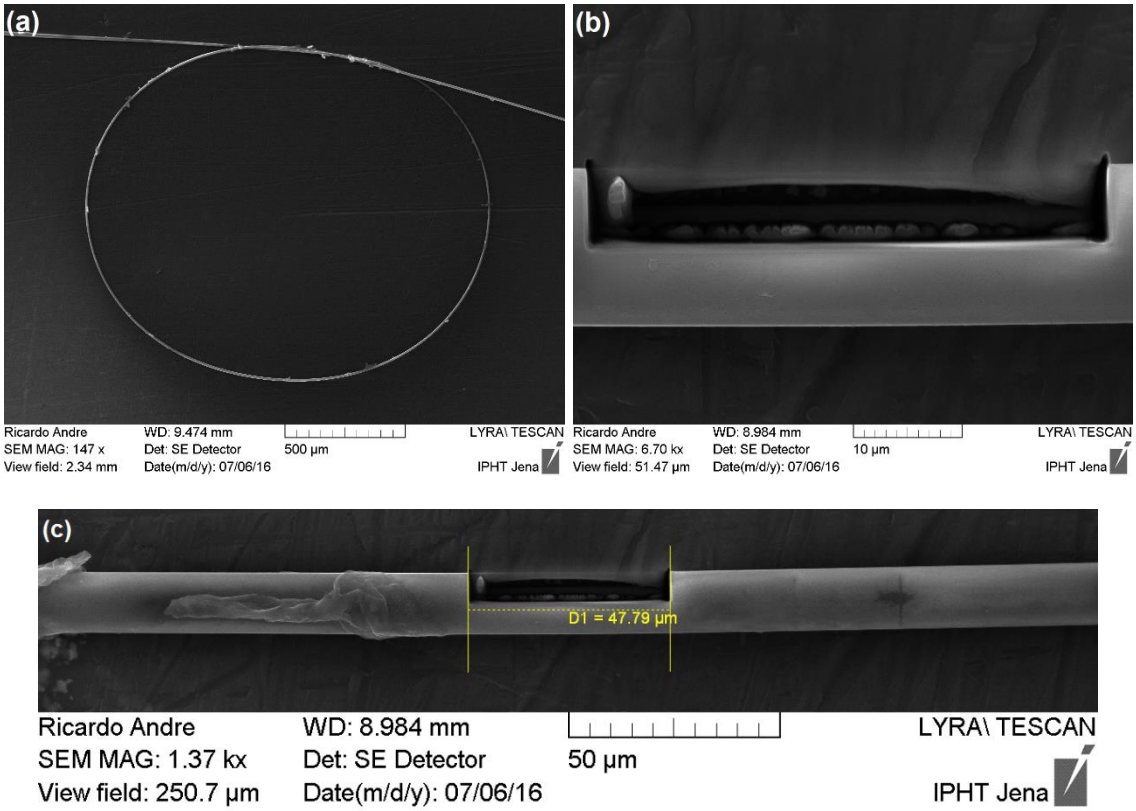

Figure 4.15. SEM images of the sensor: (a) MKR with around 700 µm-diameter; (b) Fabry-Perot cavity milled next to the MKR; (c) Fabry-Perot cavity measurement.

Figure 4.16 presents the transmission spectrum of the sensor before and after the cavity milling. After creating the cavity, the transmitted signal intensity decreased from an average of -39 dB to -46 dB at 1550 nm. The MKR spectrum is still visible after the cavity milling. However, the diameter of the MKR structure is slightly different and this is detected through a small change in the FSR.

To observe the spectrum relative to the created cavity, it is necessary to use a wider range of wavelengths. The free spectral range (FSR) for a Fabry-Perot cavity is given by [78]:

$$FSR = \frac{\lambda_1 \lambda_2}{2Ln} \qquad (6)$$

where the *FSR* is the difference between the center wavelengths of the two adjacent valleys in the interference spectrum $(\lambda_2-\lambda_1)$, *L* is the cavity length, and *n* is the cavity refractive index. Making a simple approximation by considering both λ_2 and λ_1 equal to 1550 nm and using 1.0 for the refractive index of air, a FSR of 25 nm should be obtained.

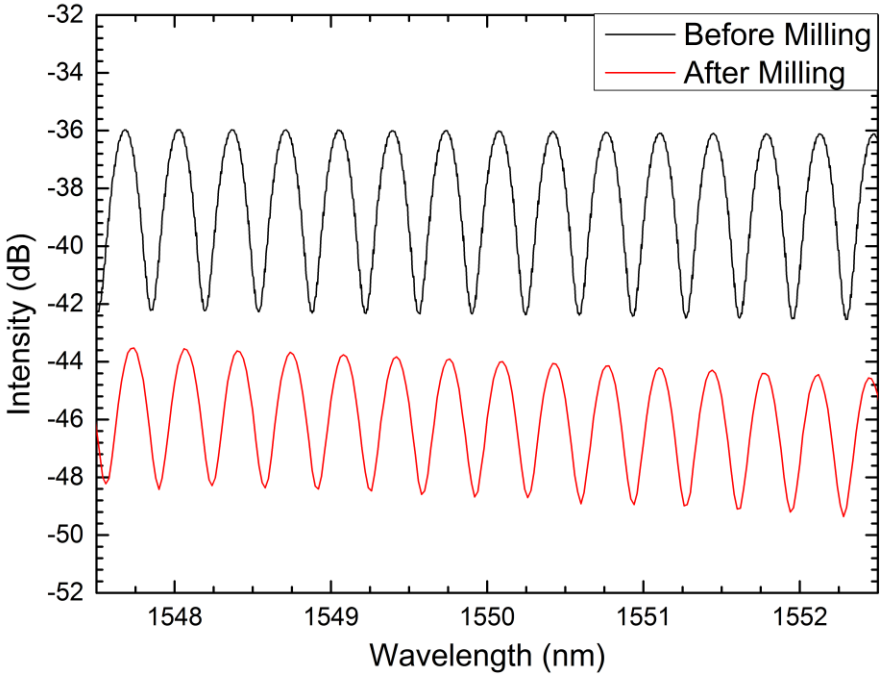

Figure 4.16. Transmission spectrum of the sensor in air before and after milling the Fabry-Perot cavity (MKR component).

The transmission spectrum of the sensor was measured in a wider range of wavelengths with a supercontinuum source. The result is shown in Figure 4.17. After analyzing the transmission spectrum, it appears that the FSR obtained (105 nm @ 1550 nm) is much higher than the calculated (25 nm @ 1550 nm).

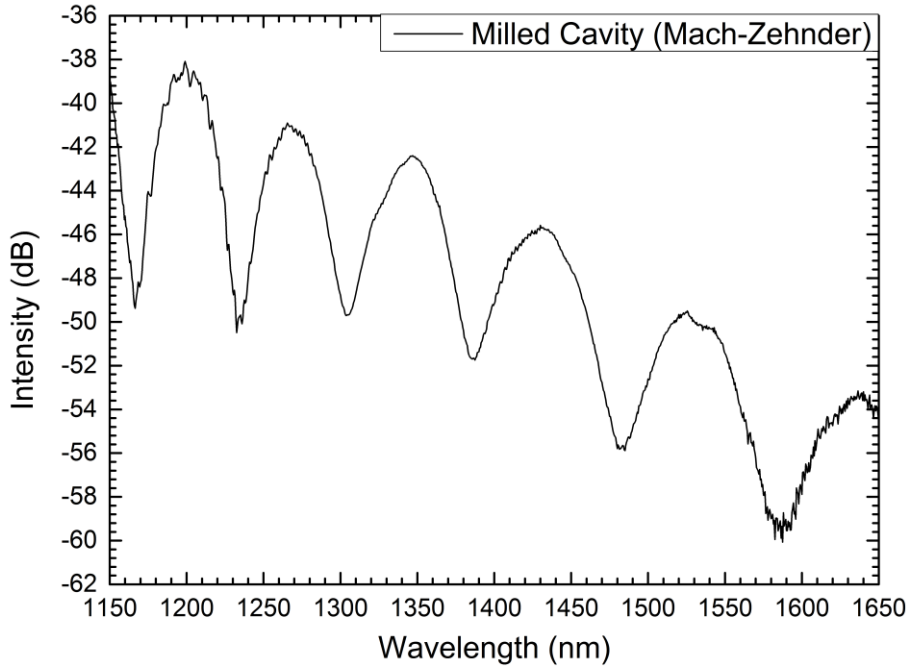

Figure 4.17. Transmission spectrum of the sensor in air after milling (cavity component).

A deeper analysis on the result shows that the cavity interference spectrum matches with the response of a Mach-Zehnder interferometer (MZI), where part of the light travels through the air cavity and the other part through the silica fiber, as exemplified in Figure 4.18. The FSR of a Mach-Zehnder is given by:

$$FSR = \frac{\lambda_1 \lambda_2}{L\Delta n} \quad (7)$$

where λ_2 and λ_1 are the central wavelengths of the two adjacent valleys in the interference spectrum, *L* is the cavity length and Δn is the refractive index difference between the two different optical paths. In this case, Δn is the difference between the refractive index of silica (n=1.444 @ 1550 nm) and the air cavity refractive index (n=1.0). Considering the two peaks around 1550nm, λ_1 and λ_2 are respectively 1483 nm and 1586 nm. Therefore, the calculated FSR is 110 nm.

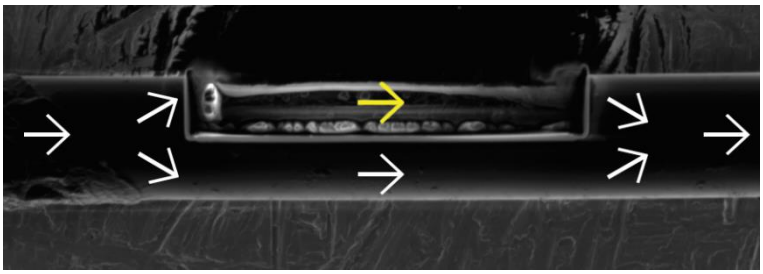

Figure 4.18. Light path in the MZI cavity structure.

The MZI cavity was submitted to different refractive index solutions in order to determine the refractive index sensitivity of this structure. The phase difference between the silica arm and the cavity arm of the interferometer will be affected by the refractive index of the cavity. This phase difference can be expressed as:

$$\Delta\phi = \frac{2\pi}{\lambda}\Delta nL \quad (8)$$

where $\Delta n = n_s - n_c$ is the refractive index difference between the two optical paths (silica and cavity). The refractive index sensitivity is the relation between the wavelength shift and the refractive index variation (in this case, the cavity refractive index (n_c)) which can be translated as $\delta\lambda/\delta n_c$. However, to simplify the calculations, the inverse can be calculated:

$$\frac{\delta n_c}{\delta\lambda} = \frac{\delta n_c}{\delta\Delta\phi}\frac{\delta\Delta\phi}{\delta\lambda} \quad (9)$$

Using equation (8), the following results are obtained:

$$\frac{\delta n_c}{\delta \Delta\phi} = -\frac{\lambda}{2\pi L} \qquad (10)$$

$$\frac{\delta \Delta\phi}{\delta \lambda} = -\frac{2\pi}{\lambda^2}\Delta n L + \frac{2\pi}{\lambda}\frac{\delta \Delta n}{\delta \lambda} L \qquad (11)$$

Replacing (10) and (11) in equation (9):

$$\frac{\delta n_c}{\delta \lambda} = \frac{\Delta n}{\lambda} - \frac{\delta \Delta n}{\delta \lambda} = \frac{n_s - n_c}{\lambda} - \frac{\delta n_s}{\delta \lambda} + \frac{\delta n_c}{\delta \lambda} \qquad (12)$$

The chromatic dispersion of silica $\delta n_s/\delta\lambda$ is around -1.3324x10^{-5} nm^{-1} @ 950 nm[3] and the used refractive index solutions are mostly composed of water, which have approximately -2x10^{-5} nm^{-1} @ 950 nm of chromatic dispersion ($\delta n_c/\delta\lambda$). The refractive index sensitivity of the MZI cavity ($\delta\lambda/\delta n_c$) should be:

$$\frac{\delta \lambda}{\delta n_c} = \frac{1}{\frac{n_s - n_c}{\lambda} - \frac{\delta n_s}{\delta \lambda} + \frac{\delta n_c}{\delta \lambda}} \qquad (13)$$

The deduction was based on the geometrical structure of the sensor, not considering the real effective refractive indices. However, it is good enough to obtain an order of magnitude for the absolute value of the sensitivity.

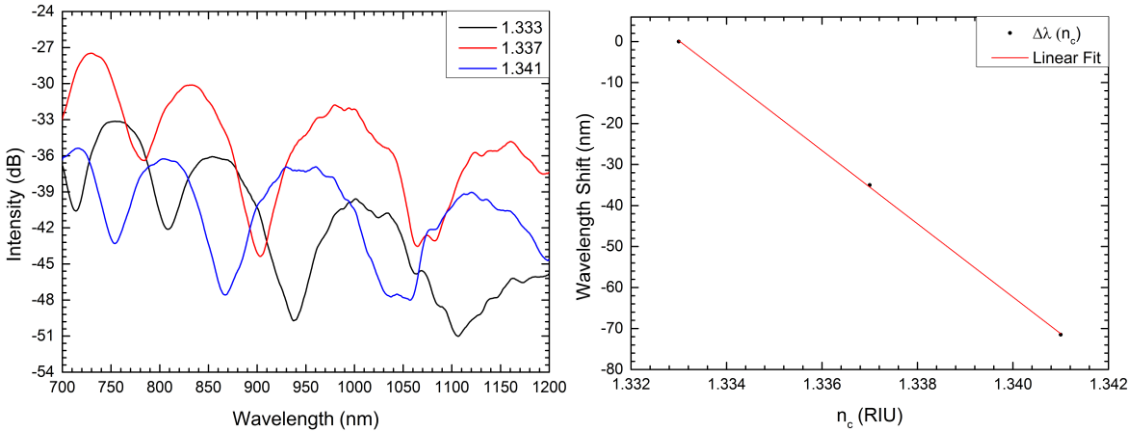

Figure 4.19. On the left: transmission spectrum of the MZI cavity under different refractive index solutions. On the right: wavelength shift as a function of the cavity refractive index (n_c).

[3] Value obtained from www.refractiveindex.info

For a cavity filled with water and measuring in a wavelength around 950 nm, where the refractive index of silica and water are respectively 1.4511 and 1.3270, the refractive index sensitivity should be 8067 nm/RIU. Note that the sensitivity is not linear, but it can be considered approximately linear in a short refractive index range.

Due to a lack of refractive index solutions, the sensor was only dipped in 3 sodium chloride solutions with refractive indices 1.333, 1.337 and 1.341 @ 1550 nm. The sensor spectrum under these solutions is shown in Figure 4.19. The wavelength shift around 950 nm was monitored as a function of the cavity refractive index. The result is also depicted in Figure 4.19. A preliminary result of -8935 ± 108 nm/RIU is obtained for the refractive index sensitivity, which is higher than the calculated one. This difference may be due to a bad calibration of the solutions, incorrect values of chromatic dispersion for silica and for the solution (a slight change in these values can lead to considerable changes in the sensitivity) or even the lack of data points.

4.2.3 Discussion

Using a FIB system, the idea of incorporating Fabry-Perot cavities in MKR structures was explored with the final purpose of achieving simultaneous measurement of refractive index and temperature by monitoring the joint response of these sensors. To do so, 3 Fabry-Perot cavities were created.

A first cavity, 40 µm-wide, was milled on the top of a MKR with around 4.5 mm-diameter. This MKR was made using a 27 µm-diameter taper which was fabricated using a CO_2 technique, as explored before. The taper presents a transmission spectrum with an interference pattern originated by the abrupt transition regions. The interference pattern has proven to remain slightly after the creation of a MKR using the taper. During the milling process, the milling area needed to be constantly adjusted due to movements of the MKR structure. This can easily introduce defects and makes it impossible to perform a good polishing of the cavity surfaces, which is crucial for this device. In a not well polished surface, the irregularities induce light scattering which consequently bring high losses to the system. Moreover, the tantalum coating used to eliminate charging effects absorbs some light and also introduces losses. The transmission spectrum of the device was measured and a low intensity noisy signal was obtained.

The losses introduced by the tantalum coating were studied by sputtering tantalum in a 4.2 mm-diameter MKR. The spectrum after the sputtering is at noise level, showing that the tantalum coating is a limiting problem.

A second cavity, also 40 µm-wide, was created on the top of a 1.6 mm-diameter MKR with the same characteristics as the first one. The MKR structure was fixed to the holder with silver paint in the ring region of the MKR. This method avoids the movement of the structure during the milling process but, in other hand, introduces some losses since the silver paint is now in the taper region and not in the SMF region. The structure moved slightly during the process using this method, which was enough to polish the cavity surface. Before sputtering, the whole structure was covered except a small part in the MKR ring where the silver paint is located, allowing the deposition of tantalum only in the exposed area. In the end, the coating was removed using the FIB, minimizing the losses.

Despite all the care in relation to losses and structure movement, the sensor broke in the cavity position while removing the silver paint with a droplet of acetone, showing the infeasibility of the structure. This scenario was in some way expected, since the cavity is like a fracture created in a glass structure that is under tension and, therefore, likely to break.

Two alternatives were introduced: creating 2 small rips in the MKR structure to form a silica cavity, or create the same Fabry-Perot cavity as before but in the taper region next to the MKR. In the first alternative, the silica cavity should be highly independent of the refractive index, but sensitive to temperature, while the MKR structure should be more sensitive to refractive index and also sensitive to temperature. Therefore, there is the possibility to discriminate between refractive index and temperature because both structures will have different responses to these parameters. However, by the same logic as before, this first alternative is likely to break since it is also a fracture in a MKR structure that is under tension, while in the second alternative, the taper region next to the MKR is not under tension. Regarding this, the second alternative was explored.

A 47.8 µm-wide Fabry-Perot cavity was created in the taper region next to a 700 µm-diameter MKR. The used taper was produced with 11 µm-diameter using the VYTRAN machine. The transition regions of this taper are very smooth, which means that the taper had low losses compared with the tapers fabricated with the available CO_2 laser system. The taper region next to the MKR structure was fixed with silver paint and, using the knowledge gained previously, only this area was covered with tantalum coating to reduce the losses.

The detected intensity decreased from -39 dB to -46 dB at 1550 nm, after milling, due to losses introduced by the cavity. The MKR interference spectrum was maintained, despite being slightly changed due a small change in the diameter of the ring. Using a

supercontinuum source, the transmission spectrum was measured. The result is an interference pattern modulating the MKR response. This interference pattern is caused by the cavity.

For this Fabry-Perot cavity, a theoretical FSR of 25 nm @ 1550nm was calculated. However, the measured FSR was 105 nm @ 1550 nm, which reveals that the cavity does not behave like a Fabry-Perot cavity as first expected. A deeper analysis showed that the cavity behaves as a Mach-Zehnder interferometer, where light travels though the cavity and also through the silica part below the cavity, interfering in the end due to the accumulated phase difference between the two waves. A FSR of 110 nm @ 1550nm was calculated for a Mach-Zehnder interferometer with this characteristics, which is similar to the measured one (105 nm @ 1550 nm).

A theoretical analysis was performed in order to obtain an expression for the absolute value of the sensitivity of the Mach-Zehnder interferometer cavity. A sensitivity of 8067 nm/RIU @ 950 nm was calculated for a cavity refractive index around 1.3270 @ 950 nm (water). The expression for the sensitivity is not linear, but one can always assume a linear approximation in a short refractive index range. The sensitivity increases with wavelength, which means that the wavelength shift is greater when measuring at longer wavelengths. Moreover, the sensitivity depends on the inverse of the refractive index difference between the silica and the cavity. Hence, for refractive index solutions near the refractive index of silica the sensitivity is higher (the refractive index difference is very small). In short, the sensitivity can reach very high values when measuring solutions with a refractive index close to the silica at long wavelengths.

Due to a lack of refractive index solutions, a preliminary result of -8935 ± 108 nm/RIU @ 950 nm was obtained for the refractive index sensitivity of this cavity by dipping the sensor in 3 sodium chloride solutions with refractive indices of 1.333, 1.337 and 1.341 @ 1550 nm. This is a preliminary result since only 3 points were measured and the solutions were not well calibrated. However, it is clearly visible that this sensor has high sensitivity to refractive index.

For the future, the characterization of this sensor (MKR plus cavity) should be performed in terms of refractive index and temperature, exploring the possibility of simultaneous measurement of these two parameters. According to the theoretical expression for the refractive index sensitivity of the Mach-Zehnder interferometer cavity, the sensitivity is independent of the length of the cavity. Hence, a study should be performed to analyze the losses as a function of the cavity length.

Moreover, it should be interesting to coat just the MKR structure with low index polymer. Apart from maintaining the MKR structure more stable, it would make the sensor insensitive to the external refractive index and it would increase its temperature sensitivity.

Despite the high probability of breaking, the idea of creating two rips in the MKR ring to form a silica cavity should also be explored.

Chapter 5

Fiber Bragg Grating on Abrupt Tapered Tip

FBGs in conventional core-cladding fiber are insensitive to changes in the external refractive index since they are not directly exposed to the outside medium. However, sensitivity can be gained by either thinning or etching the fiber before or after the FBG inscription [46], or by using suspended core fibers [69].

FBGs have been used for refractive index sensing for two decades [91], [92]. Then, multiple configurations using this structure were studied and developed for the same purpose, such as: FBG Fabry-Perot cavities [93], Fabry-Perot cavities based on high-birefringence FBG [25], FBG in microstructured optical fibers [94]–[96], and focused ion beam-milled FBG in tapered fibers [97].

In this chapter, an FBG inscribed on an abrupt tapered fiber tip is explored for refractive index and temperature sensing. The tip was obtained from an abrupt taper, with 18 µm waist, fabricated with a CO_2 laser. A phase-mask interferometer with a femtosecond laser [70] was used to inscribe the Bragg grating in the taper waist region.

5.1. Fabrication and Characterization

The abrupt taper, with 18 µm diameter waist and a length of 40 mm, was fabricated using a CO_2 laser technique. In order to create the abrupt transition region, a constant tension was applied to the fiber from the beginning until the end of the whole taper production process. For this taper, the abrupt taper transition was around 300 µm in length.

An FBG was then inscribed in the taper using the same phase-mask interferometer driven by an ultraviolet femtosecond laser (267 nm) as used in section 4.1.1.

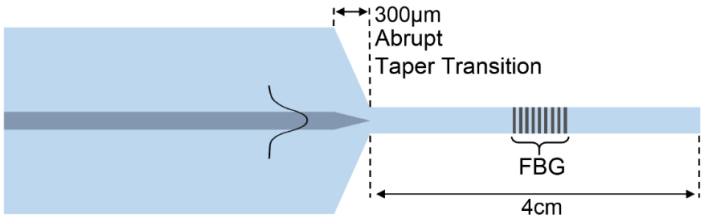

Figure 5.1. Schematic of the sensor tip.

Regarding the dimensions of the taper waist (18 µm), the setup was adjusted to obtain a reflection wavelength of the fundamental mode near 1550 nm by using a

diffraction mask with a period of 1075 nm. Since the taper has an 18 μm-diameter waist, it is mainly composed of pure silica (n=1.444 @ 1550 nm), which has less photosensitivity than doped silica. Hence a long inscription time of 10 minutes was used. A laser power of 200 mW was used during the inscription. The taper was then broken at one of the transition regions in order to create the tip.

Figure 5.1 shows a schematic of the FBG inscribed in the abrupt fiber taper tip. To measure the sensor spectrum in reflection, an optical circulator and a broadband source with a central wavelength of 1550 nm and a bandwidth of 100 nm was used. The broadband source was connected to the optical circulator and the reflection spectrum was observed in an optical spectrum analyzer (OSA) with 0.02 nm resolution.

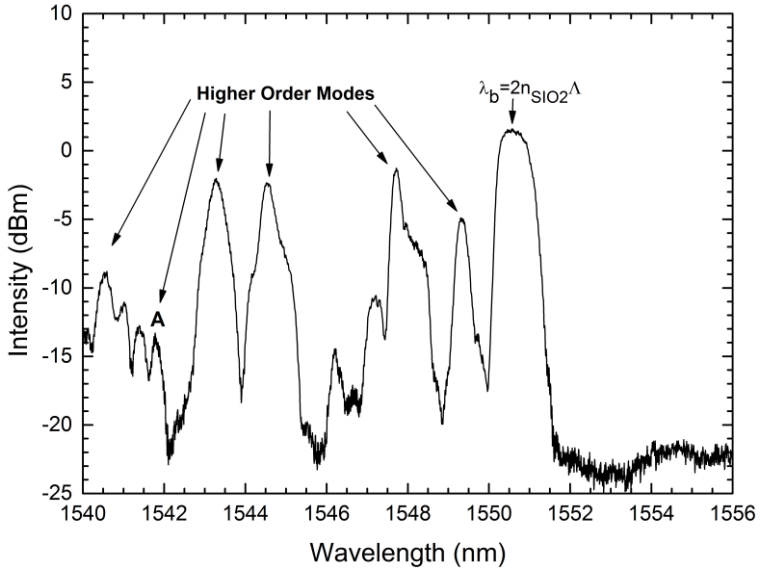

Figure 5.2. Reflection spectrum of the sensor in air.

The reflection spectrum of the sensor in air is presented in Figure 5.2. The fundamental mode peak is centered at 1550.6 nm and it should have an effective refractive index next to pure silica (n=1.444 @ 1550 nm). Since the Bragg grating period is 537.5 nm and the reflection peak is centered at 1550.6 nm, according to equation (5) the effective refractive index of the fundamental mode should be 1.442[4].

Due to the abrupt transition region of the taper tip, many modes with different effective refractive indices are excited providing reflections at different wavelengths. These reflection peaks will, in principle, extend until a Bragg wavelength of 1075 nm,

[4] Comparison with simulated effective refractive index in Appendix B.2.

which corresponds to the refractive index of air (a “mode” propagating in air). The considered reflection peak A is centered at 1541.8 nm, which corresponds to an effective refractive index of 1.434 according to Bragg’s law.

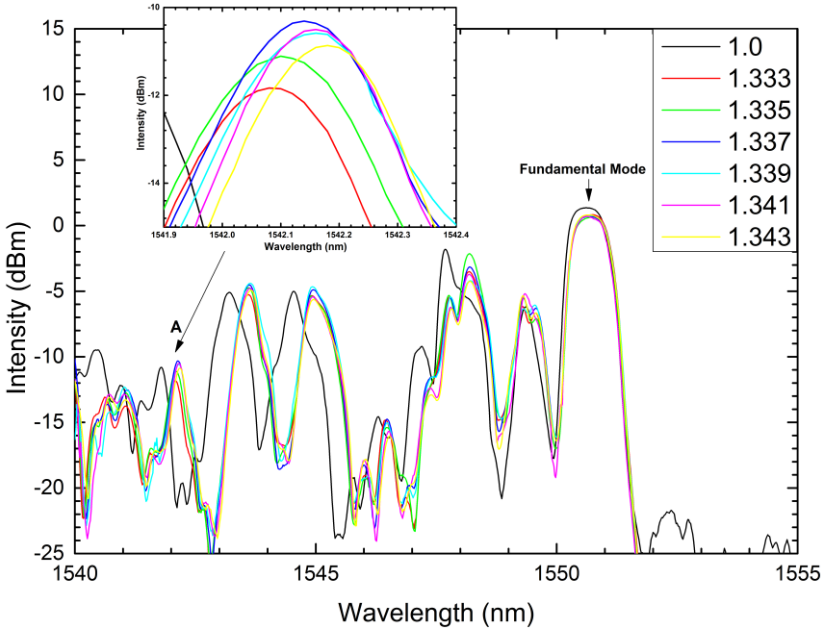

Figure 5.3. Reflection spectrum of the sensor immersed into solutions with different refractive indices. The inset is a zoom of a high order mode reflection peak (peak A).

Refractive index sensing of liquids was studied using this sensor. Several solutions of water with sodium chloride at different concentrations were used, resulting in a refractive index range from 1.333 to 1.343, with a step of 0.002 RIU (refractive index units). The sensing tip was immersed in each solution and the wavelength shift for the fundamental mode and a higher order mode A were measured.

Theoretically, the fundamental mode will be less sensitive to refractive index changes than higher order modes since the optical field is more confined within the taper, hence less affected by the external medium. A measurement of the amount of field that is inside of the taper can be obtained through the normalized propagation constant. The normalized propagation constant is given by:

$$b = \frac{n_{eff}^2 - n_{clad}^2}{n_{core}^2 - n_{clad}^2} \qquad (14)$$

where n_{eff} is the effective refractive index, n_{core} is the refractive index of the taper ($n_{core} = 1.444$) and n_{clad} is the refractive index of the external medium (in the case of air $n_{clad} = 1$). Using the calculated effective refractive indices, the normalized propagation constant is 0.995 for the fundamental mode and 0.973 for the higher order mode A. Only

3% of the electric field is outside of the taper in the higher order mode A. The higher the order of the mode (the lower the effective index), the greater the contribution of the external medium to the effective refractive index of the mode (more electric field is outside of the fiber taper). Thus, the relative sensitivity between a higher order mode peak and a fundamental mode peak can be monitored.

In Figure 5.3 is presented the sensor spectrum in reflection under different refractive index solutions. In the inset is possible to see the wavelength shift of a higher order mode peak with the refractive index change. For the higher order mode A and the fundamental mode, the wavelength shift was measured as a function of refractive index variation and the result is depicted in Figure 5.4.

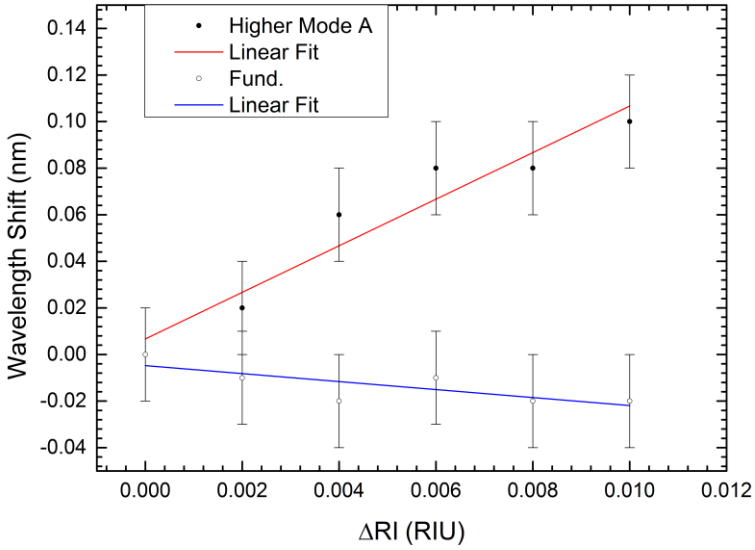

Figure 5.4. Wavelength shift as a function of refractive index variation for different modes.

Reflection Peak	RI Sensitivity
Higher Mode A	10.0 nm/RIU
Fundamental Mode	-1.3 nm/RIU

Table 5.1. Comparison of sensitivities between fundamental mode and the higher order mode A.

From the fit, a refractive index sensitivity of 10 ± 1 nm/RIU was obtained for the higher order mode peak A, in a refractive index range from 1.333 to 1.343. The fundamental mode is almost insensitive to refractive index variations, resulting in a sensitivity of -1.3 ± 0.9 nm/RIU. The resolution scale of the optical spectrum analyzer is a limitation of the measurements.

The sensing tip was also studied for temperature sensing. A Fluke Metrology Well was used to heat the sensor from 25ºC up to 200ºC.

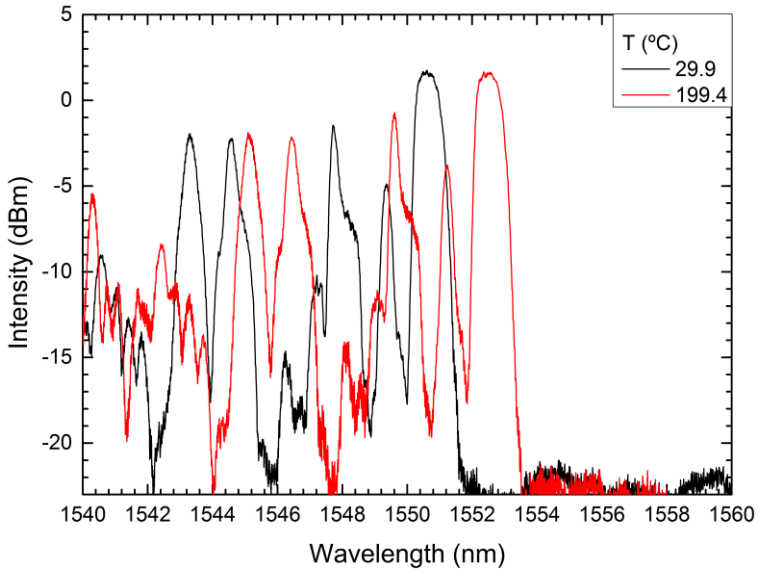

Figure 5.5. Reflection spectrum of the sensor for 2 different temperatures.

Figure 5.5 shows two of the measured spectra at different temperatures. It is expected that the fundamental mode has higher sensitivity to temperature, since the mode is more confined and hence it is more affected by the thermo-optic coefficient of silica. In the same line of thought, higher order modes will have less sensitivity to temperature.

The higher order mode peak A considered for refractive index sensing and also the fundamental mode peak were monitored as a function of temperature. The wavelength shift as a function of temperature variation for both peaks is displayed in Figure 5.6.

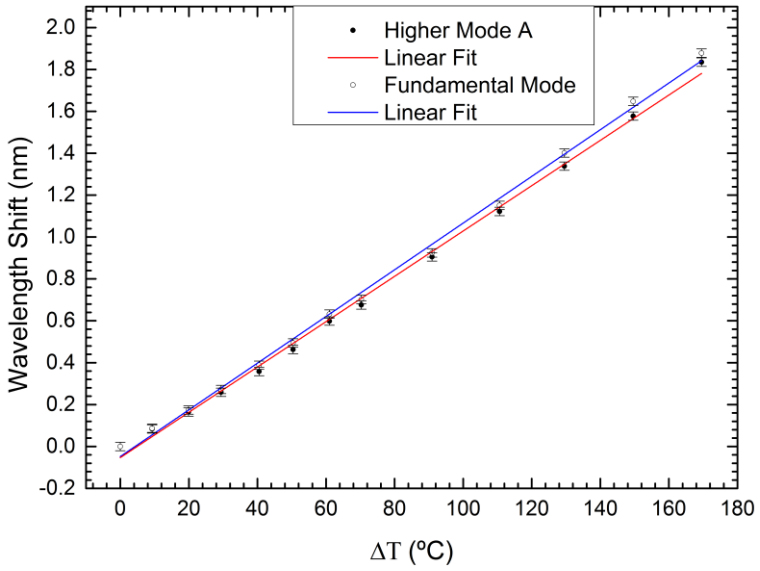

Figure 5.6. Wavelength shift as a function of temperature variation for the fundamental mode and for the higher order mode considered in the refractive index measurements.

Reflection Peak	Temperature Sensitivity
Higher Mode A	10.8 pm/ºC
Fundamental Mode	11.1 pm/ºC

Table 5.2. Comparison of sensitivities between fundamental mode and the higher order mode A.

A linear fit was performed on the data, achieving a sensitivity of 10.8 ± 0.1 pm/ºC for the higher order mode A and a sensitivity of 11.1 ± 0.1 pm/ºC for the fundamental mode.

The considered peaks have similar temperature sensitivity but different refractive index sensitivity. With this, one can use this sensor to measure refractive index with practically no influence of temperature by monitoring the difference of the wavelength shift of the two reflection peaks.

5.1.1 Temperature Independent Refractive Index Sensing

Considering $\Delta\lambda_2$ as the wavelength shift of the higher order mode reflection peak A and $\Delta\lambda_1$ as the wavelength shift of the fundamental mode reflection peak, a new analysis can be made using the difference between both wavelength shifts, $\Delta\lambda_2 - \Delta\lambda_1$.

The difference between the wavelength shift of the reflection peak A and the fundamental mode ($\Delta\lambda_2 - \Delta\lambda_1$) as a function of refractive index variation is shown in Figure 5.7 and in Figure 5.8 as a function of temperature variation.

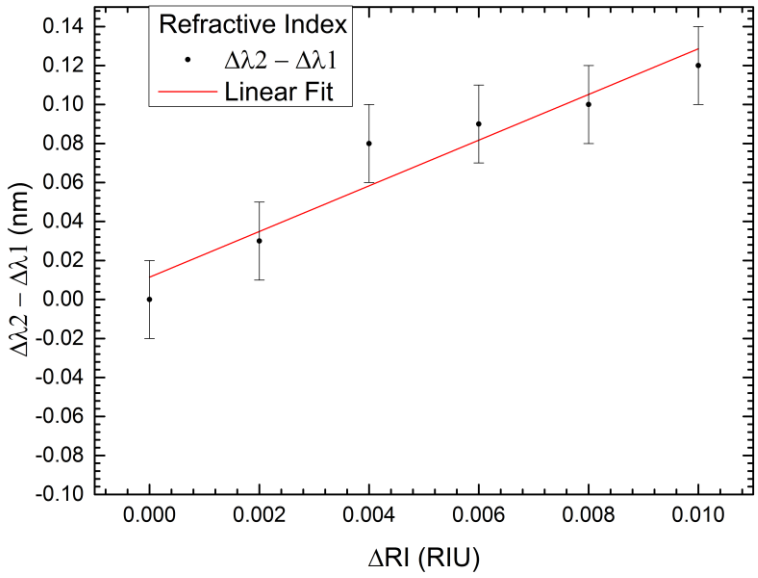

Figure 5.7. Separation between wavelength shifts ($\Delta\lambda_2 - \Delta\lambda_1$) as a function of refractive index variation.

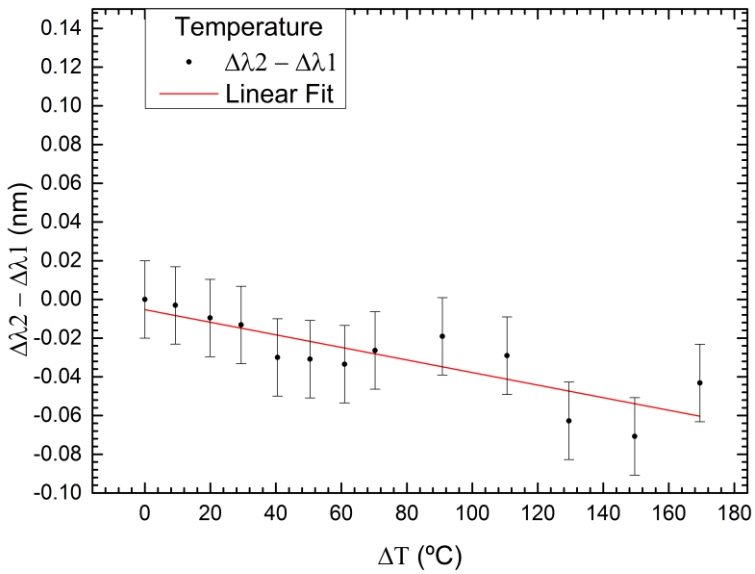

Figure 5.8. Separation between wavelength shifts ($\Delta\lambda_2 - \Delta\lambda_1$) as a function of temperature variation.

With this new analysis, the sensor presents a sensitivity of 11.7 ± 1.7 nm/RIU to refractive index and -0.32 ± 0.06 pm/ºC to temperature. Dividing both values, a cross-sensitivity of -2.7×10^{-5} RIU/ºC is obtained. Imagining a situation in which the temperature fluctuates 25 ºC during a refractive index measurement, the refractive index is only affected in the 4th decimal place (±0.0007 RIU).

5.1.2 Simultaneous Measurement of Refractive Index and Temperature

Feasibility analysis was performed on the simultaneous measurement of refractive index and temperature using this sensor. Such alternative way of measuring relies on the fact that both peaks have different sensitivities to each measured parameter. These sensitivities are used to create a matrix that is able to discriminate between the different measured parameters by analyzing the wavelength shift of each peak.

Each reflection peak will suffer a wavelength shift due to refractive index and to temperature variations according to this relation:

$$\Delta\lambda_i = \Delta n\, k_{in} + \Delta T\, k_{iT} \qquad (15)$$

where $\Delta\lambda_i$ is the wavelength shift of the reflection peak "$_i$", with i =1,2, Δn and ΔT are respectively the refractive index and temperature variations, k_{in} is the refractive index sensitivity of the reflection peak "$_i$" and k_{iT} the temperature sensitivity of the reflection peak "$_i$".

Considering two reflection peaks, the fundamental mode (λ_1) and the higher order mode A (λ_2), the expression involving the sensitivities of these peaks is $\Lambda = [K]\Omega$, which can be written in matrix form as:

$$\begin{bmatrix}\Delta\lambda_1\\ \Delta\lambda_2\end{bmatrix} = \begin{bmatrix}k_{1n} & k_{1T}\\ k_{2n} & k_{2T}\end{bmatrix}\begin{bmatrix}\Delta n\\ \Delta \mathrm{T}\end{bmatrix} \quad (16)$$

Inverting the matrix expressions to obtain the refractive index and temperature variations as a function of the wavelength shifts, one can obtain:

$$\begin{bmatrix}\Delta n\\ \Delta T\end{bmatrix} = \frac{1}{D}\begin{bmatrix}k_{2T} & -k_{1T}\\ -k_{2n} & k_{1n}\end{bmatrix}\begin{bmatrix}\Delta\lambda_1\\ \Delta\lambda_2\end{bmatrix} \quad (17)$$

where $D = k_{1n}.k_{2T} - k_{1T}.k_{2n}$. From the values given in Table 5.1 and Table 5.2, equation (17) becomes:

$$\begin{bmatrix}\Delta n\\ \Delta T\end{bmatrix} = \frac{1}{-0.12504}\begin{bmatrix}0.0108 & -0.0111\\ -10.0 & -1.3\end{bmatrix}\begin{bmatrix}\Delta\lambda_1\\ \Delta\lambda_2\end{bmatrix} \quad (18)$$

The stability of this method can be verified through the condition number of the matrix, which is a quantity that provides a qualitative estimate for the sensitivity of the solution of a system of linear equations [98].

The condition number is given by:

$$Condition\ \# = \|K\|_2\|K^{-1}\|_2 \quad (19)$$

In this case of a square matrix, the Euclidian norm can be used:

$$\|K\|_2 = \sqrt{\lambda_{max}(K^*K)} \quad (20)$$

where λ_{max} is the largest eigenvalue of the matrix K^*K (K^* is the conjugate transpose of K). The lower the condition number, the lower the error. For high condition number matrices, a small change in Λ will lead to a large error in the solution Ω. In this case, the condition number is around 900, which shows that the matrix is ill-conditioned. Ideally, a well-conditioned matrix have a condition number near 1.

5.2. Discussion

An FBG was inscribed in an abrupt taper using a phase-mask interferometer driven by a femtosecond laser. The inscribed FBG has a period of 537.5 nm, which corresponds to a Bragg wavelength of 1550.6 nm for the fundamental mode of the abrupt taper. Due to the abrupt taper transition, many modes were excited with different effective refractive indices that will be reflected at different wavelengths according to Bragg's law in equation (5). The last reflection peak should correspond to a mode where the effective refractive index is the same as the refractive index of air.

The taper was broken in one of the transition regions, obtaining an abrupt fiber taper tip with an FBG inscribed in the taper waist region. Refractive index and temperature measurements were performed using this sensor. For refractive index sensing, a sensitivity of 10 ± 1 nm/RIU was obtained in the refractive index range from 1.333 to 1.343, by monitoring the wavelength shift of a higher order mode peak. The fundamental mode peak is almost insensitive to refractive index, with a measured sensitivity of -1.3 ± 0.9 nm/RIU. The refractive index sensitivity of this peak is low and the wavelength shift is at the resolution scale of the optical spectrum analyzer, limiting the measurements. However, it is clearly visible that the higher the order of the mode, the greater the sensibility. Higher modes than the ones considered for the measurements should have more sensitivity to refractive index since the optical field is more affected by the external medium (the mode is less confined).

For temperature sensing, a sensitivity of 10.8 ± 0.1 pm/ºC was achieved for the same higher order mode peak considered for refractive index measurements. As expected, the highest sensitivity was obtained for the fundamental mode (11.1 ± 0.1 pm/ºC) because it is more confined and is more affected by the thermo-optic coefficient of silica.

Considering the difference between the wavelength shift of both measured peaks, it is possible to measure refractive index with a sensitivity of 11.7 ± 1.7 nm/RIU with low influence of temperature (-0.32 ± 0.06 pm/ºC). The cross sensitivity for this method was -2.7×10^{-5} RIU/ºC, which for variations of 25ºC the refractive index sensing is only affected in the 4th decimal place.

The proposed sensor is similar to the one presented by Ran *et al.* [99], which achieves a temperature independent refractive index sensitivity of -9.47 nm/RIU. However, the higher order mode considered in this work is greater than the one considered by Ran *et al.*, obtaining greater sensitivity to refractive index. To achieve

higher refractive index sensitivities, one should analyze reflection peaks of high order modes with lower normalized propagation constants (lower effective index) than the one considered in this paper.

A feasibility analysis was performed for the simultaneous measurement of refractive index and temperature using a matrix method to discriminate between these two parameters. It was determined that the matrix is ill-conditioned for the parameters used, which is due to the fact that the temperature sensitivities of both modes are practically the similar. In future, a greater discrimination in temperature sensitives could be achieved by exciting even higher order modes, which may allow this method to be successfully implemented.

Chapter 6
Final Conclusions and Future Work

The focus of this dissertation is the study of new sensors based on tapers, namely knot resonators and interferometric sensors, and the main objectives were accomplished. A Mach-Zehnder based on a large knot fiber resonator configuration is proposed for measuring refractive index of liquid solutions. An FBG has been embedded in a MKR structure. The resulting reflection spectrum has proven to be the combination of the reflection spectra of both devices. A Fabry-Perot cavity has been successfully incorporated in a MKR with the objective of achieving simultaneous measurement of 2 parameters (refractive index and temperature), by monitoring the joint response of both structures to these parameters. However, the structure has broken proving to be fragile and unviable. Two alternatives to this configuration are also proposed, namely the introduction of 2 small rips in the MKR structure, creating a silica cavity, or the creation of a Fabry-Perot cavity in the taper region next to the MKR. This last alternative has been explored and the MKR spectral response has proven to maintain after the cavity milling, which is essential for the final objective of the sensor. The created cavity behaves as a Mach-Zehnder interferometer and not as a Fabry-Perot, as first expected, and presents high sensitivity to refractive index. An FBG has also been inscribed in an abrupt taper using a phase-mask interferometer driven by a femtosecond laser. This sensor is used for temperature insensitive refractive index measurements. The viability of the sensor for simultaneous measurement of refractive index and temperature is also analyzed.

The paper *"Mach – Zehnder Based on Large Knot Fiber Resonator for Refractive Index Measurement"* has been written and published in IEEE Photonics Technology Letters in June 2016 [100], and the paper *"Fiber Bragg Grating on Abrupt Tapered Tip for Temperature Independent Refractive Index Measurement"* has been submitted to IEEE Sensors Journal.

For the Mach-Zehnder based on a large knot fiber resonator, the sensor shows higher sensitivity (642 nm/RIU) than most of the MZI and MKR configurations and works in a wide refractive index range (1.3735 to 1.4280) detecting refractive indices closer to silica, a RI region where the other configurations cannot reach. The refractive index sensitivity is similar to a biconical fiber taper [9], but in terms of temperature sensitivity is very different.

The FBG embedded in the MKR structure opens the possibility to perform simultaneous measurement of different parameters, as well as to explore the influence of curvature in the FBG structure by varying the diameter of the MKR. During the cavity milling study, some techniques and procedures have been developed to minimize the sensor losses. A theoretical expression for the sensitivity of the cavity is explored and proved to be independent of the cavity length. A preliminary result of -8935 ± 108 nm/RIU @ 950 nm was obtained for the cavity sensitivity in a refractive index range of 1.333 to 1.341.

As for the FBG inscribed in the abrupt taper, a refractive index sensitivity of 11.7 ± 1.7 nm/RIU was obtained in a refractive index range of 1.333 to 1.341. This value is obtained by analyzing the difference between wavelength shift of the fundamental mode and the considered higher order mode peak to make it temperature insensitive. A cross sensitivity of -2.7×10^{-5} RIU/ºC was achieved. The application of this sensor to simultaneous measurement of refractive index and temperature is not viable.

This work has left some unexplored parts and opened new doors for research in this area. To continue this work the following points should be studied:

- Investigate, in the case of the Mach-Zehnder based on a large knot resonator, the influence of the number of contact points in the knot in the signal spectrum, as well as determine if there is any predominance of one contact point over the other;
- Characterize the FBG embedded in the MKR in terms of refractive index and temperature and explore the possibility of simultaneous measurement of these parameters;
- Study the FBG embedded in the MKR spectral response as a function of the MKR curvature/diameter;
- Fully characterize the Mach-Zehnder cavity in refractive index and temperature, and study the influence of the cavity length in the sensor losses. This work is likely to be published because there are similar Mach-Zehnder sensors made using femtosecond laser milling [79], [101] but not with FIB milling. The use of FIB milling can possibly create these sensors with low losses since the polishing of the cavity surfaces is possible;
- Explore the idea of coating the MKR next to the Mach-Zehnder cavity in order to make it insensitive to refractive index, more sensitive to temperature and also more stable;

- Study the idea of creating two rips in the MKR ring to form a silica cavity and characterize it in terms of refractive index and temperature;
- Investigate the excitation of even higher order modes in the FBG inscribed in the abrupt fiber taper tip and analyze the viability of monitoring one of those modes, farther from the fundamental mode, to perform simultaneous measurement of refractive index and temperature.

Appendices

A. Microfiber Knot Resonator Simulation Using a Ring Resonator Structure

The simulation of a microfiber knot resonator (MKR) can be very difficult due to the inherent problem of simulating the knot structure. In this case, a 3D approach should be used. However, even simulating in 3D the whole design of the knot structure can be quite hard. Moreover, simulating in 3D can easily overwhelm the computer RAM and it can also take some hours to perform the simulation.

To avoid such approach, the possibility of obtaining the MKR response by simulating a ring resonator with the same characteristics as the MKR will be studied.

A.1 Theoretical Analysis

According to Lim *et al*. [102], the transmission coefficient in amplitude of a microfiber knot resonator is given by:

$$T_{Knot} = \frac{\exp\left(-\frac{\alpha L}{2}\right)\exp(j\beta L) - \sin(K)}{1 - \exp\left(-\frac{\alpha L}{2}\right)\exp(j\beta L)\sin(K)} \quad (21)$$

where α is the attenuation coefficient in intensity (that is why it is divided by 2 to be in amplitude), β is the propagation constant, L is the round-trip length. $sin(K)$ is the coupling ratio, related to the coupling length by $K = \kappa l$, where κ is the coupling constant and l is the coupling length.

Looking now into the transmission coefficient in amplitude for a ring resonator [68], [103], it is given by:

$$T_{Ring} = \frac{-\alpha' + t\exp(-j\theta)}{-\alpha' t^* + \exp(-j\theta)} \quad (22)$$

where α' is a loss coefficient, which for zero losses $\alpha' = 1$. In this expression α' is related with the incident and transmitted field by $E_i = \alpha' e^{j\theta} E_t$, being $\alpha' = \exp(-\frac{\alpha L}{2})$ as in the case of the MKR. t is the coupling parameter given by $t = |t|\exp(j\varphi_t)$, where $|t|$ represents the coupling losses and φ_t is defined as the coupling phase. The phase θ is the propagation phase given by $\theta = \beta L$. Hence, the transmission coefficient in amplitude is:

$$T_{Ring} = \frac{-\exp(-\frac{\alpha L}{2}) + |t|\exp(j\varphi_t)\exp(-j\beta L)}{-\exp(-\frac{\alpha L}{2})|t|\exp(-j\varphi_t) + \exp(-j\beta L)} \quad (23)$$

Multiplying and dividing by $\exp(j\beta L)$, the transmission coefficient in amplitude is now given by:

$$T_{Ring} = -\frac{\exp(-\frac{\alpha L}{2})\exp(j\beta L) - |t|\exp(j\varphi_t)}{1 - \exp(-\frac{\alpha L}{2})\exp(j\beta L)|t|\exp(-j\varphi_t)} \quad (24)$$

At first sight, equations (21) and (24) for the MKR and the ring resonator transmission coefficient in amplitude seem similar. Assuming that there is no coupling losses, $|t|$ is 1. Then, the only difference between both equations is the minus signal and the $\exp(j\varphi_t)$ factor. These values are simply phase terms and they should be related with the $sin(K)$ from equation (21). K and φ_t may not be the same but they have the same meaning: they are the phase due to the coupling.

Hence, it should be possible to simulate a ring resonator with the same characteristics as a MKR and obtain the response of a MKR. However, it may be needed to adjusting the coupling length to compensate some phase mismatch.

A.2 COMSOL Multiphysics Simulation

COMSOL Multiphysics is a simulation platform for advanced numerical methods to analyze and simulate physics based problems. The software uses the finite element method and, depending on the physics model (acoustic, fluids, heat transfer, optics, mechanics, semiconductors, and others), it has implemented all the necessary equations for the simulation. In this case, COMSOL Multiphysics version 4.4 was used.

To simulate the ring resonator, a 2D Electromagnetic Waves, Frequency Domain model from the Wave Optics module was chosen. This model allows to solve time-harmonic electromagnetic field distributions, which is good to see for example the transversal electric field distribution. In this model, the Boundary Mode Analysis and the Frequency Domain study were selected.

The Boundary Mode Analysis calculates a desired number of modes in the input/output of the system. The Frequency Domain study allows the program to propagate in the designed system the previously calculated modes, finishing the simulation process.

A ring resonator structure was built to simulate a MKR based on a published paper from Xiao *et al.* [4] They produced a MKR with 46 μm-diameter using a 1 μm-diameter

taper. To reproduce such device as a ring resonator, a taper distanced from a ring was simulated. The taper has a thickness of 1 µm and the ring has a diameter of 46 µm, also with a thickness of 1 µm. To complete the simulation, this structure was involved in an 8 µm-thick air cladding to simulate the MKR structure in air. The gap between the taper and the ring should be small and it was optimized to compensate any phase mismatch between the ring resonator structure and the published MKR, as explored back in A.1. In this case, the gap was set to 600 nm.

The simulated structure is presented in Figure 0.1. The region in blue is the ring resonator structure and it was defined as silica (n=1.444 @ 1550 nm). The gray region was defined as air (n=1.00). The software has a database with several materials with all the physical constants, including the refractive index.

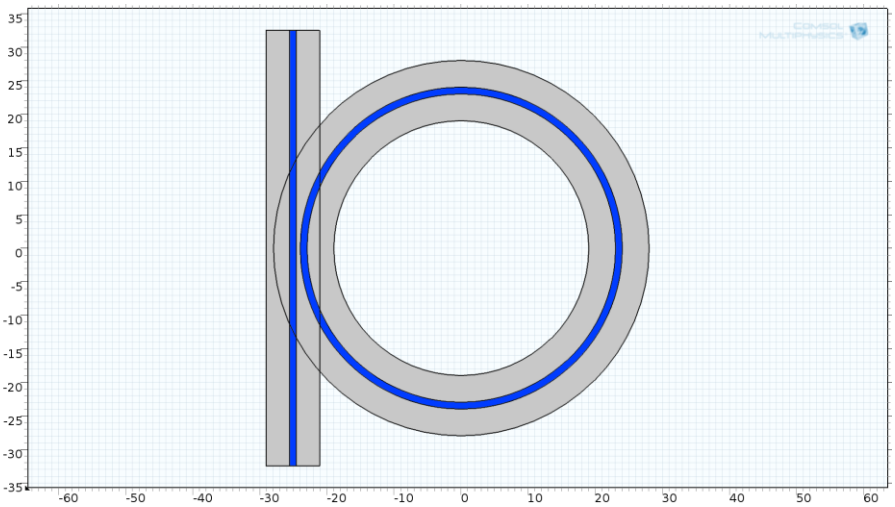

Figure 0.1. Ring structure simulated. Blue: 1 µm-diameter fiber taper and ring. Gray: air.

For the electric field to be physically correct, a scattering boundary condition was applied to the outer part of the system, except the input and output ports. This avoids the electric field to be back scattered in the outer boundary and interfere originating an incorrect result. The input port is the bottom taper end and the output port the top taper end. The mesh was defined manually, being more refined in the blue region, as well as in the gap zone.

The simulation began with the Boundary Mode Analysis in the input and output ports. It was defined to calculate the fundamental mode at this ports searching for the effective refractive index around the refractive index of silica. Then, the Frequency Domain study will propagate the fundamental mode through the system with a frequency defined as c/λ, where c is the speed of light in vacuum, determining the transversal electric field distribution.

A wavelength sweep was performed for values between 1540 nm and 1570 nm. To obtain the transmittance, a probe was created to collect at each wavelength the input (E_i) and the output electric field (E_o), calculating $|E_o/E_i|^2$. The simulated transmittance is depicted in Figure 0.2.

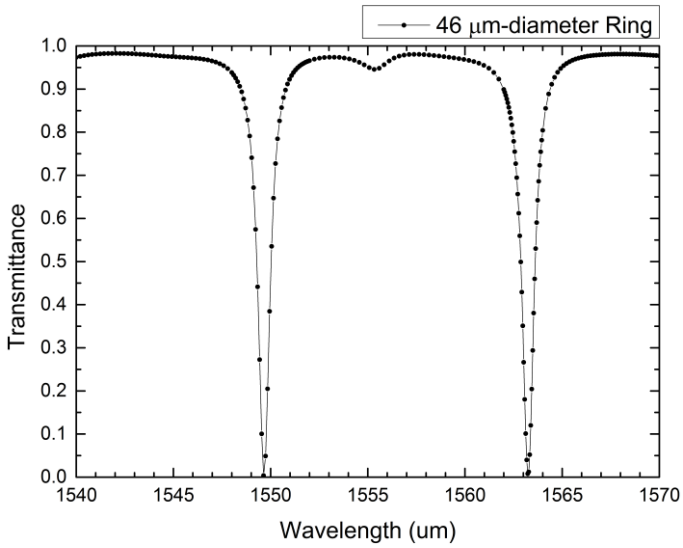

Figure 0.2. Transmittance spectrum of the simulated ring resonator.

The result is plotted in a logarithmic scale in Figure 0.3, together with the transmission spectrum of the published MKR with the same characteristics.

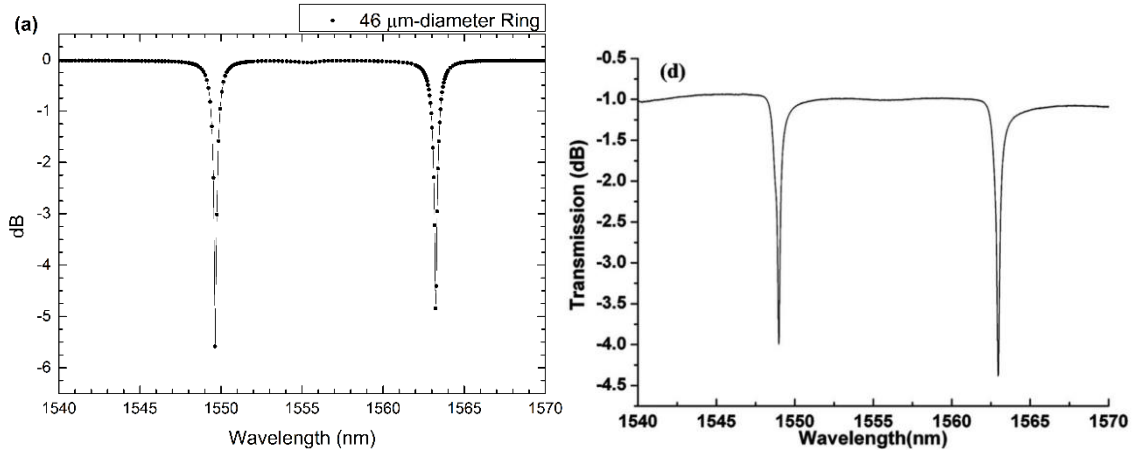

Figure 0.3. Transmission spectrum of the simulated ring resonator and the published MKR respectively on the left (a) and right (d).

The resonance peaks from the simulated ring resonator match the resonance peaks from the MKR with the same dimensions. Hence, it is possible to predict the resonant wavelengths of a MKR by simulating a ring resonator with the same dimensions. The ring resonator was considered lossless, that is why the transmission losses of the ring resonator in a wavelength out of resonance is approximately zero.

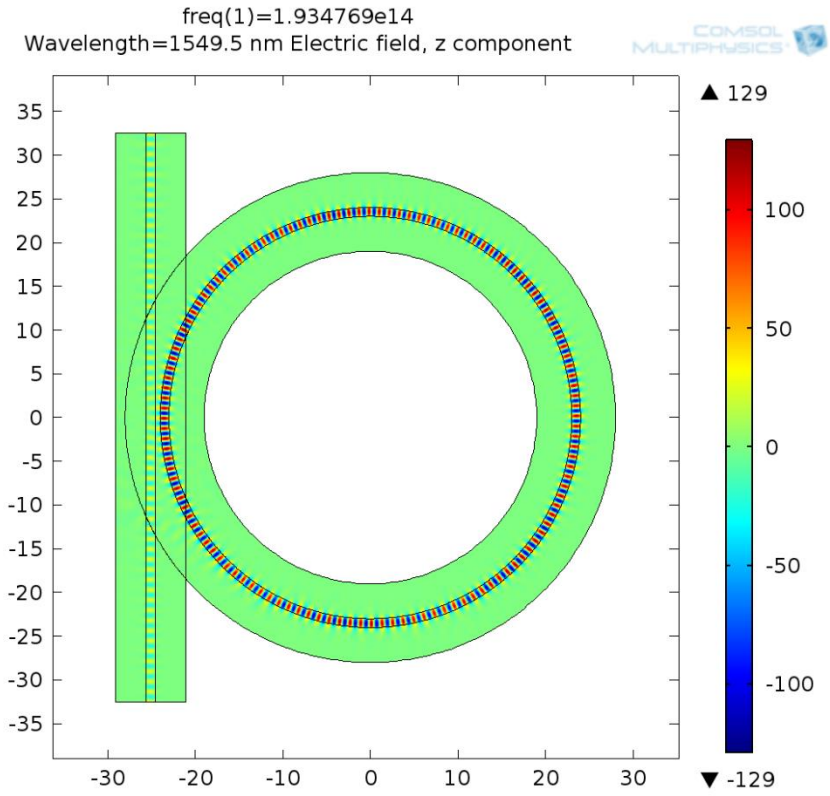

Figure 0.4. Transversal electric field distribution at a resonant wavelength (1549.5 nm). The electric field units are in KV/m.

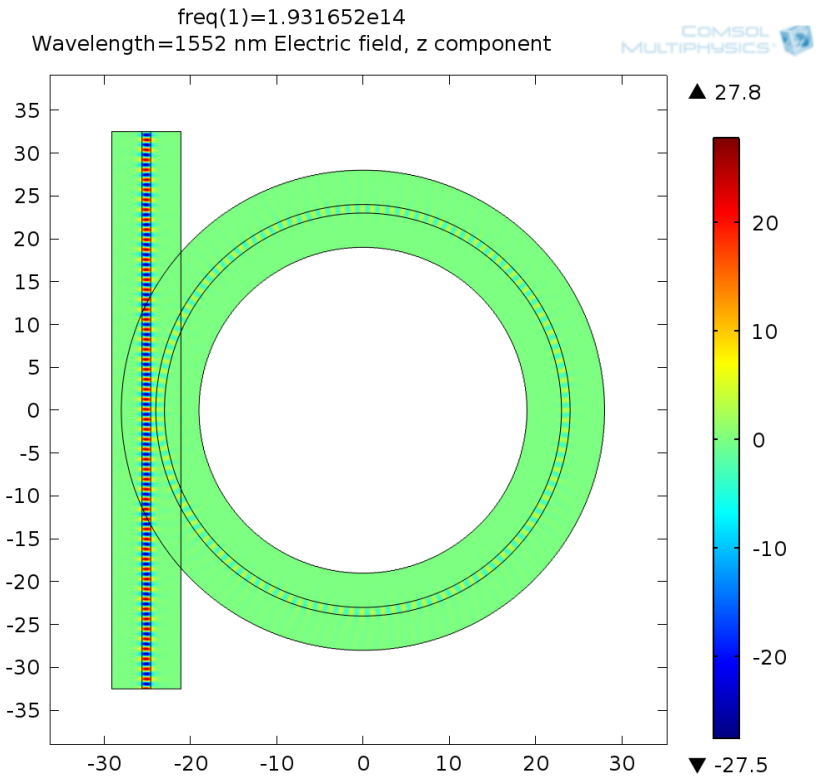

Figure 0.5. Transversal electric field distribution in a situation out of resonance (1552 nm). The electric field units are in KV/m.

The transversal electric field distributions in a resonance situation is plotted in Figure 0.4 and in a situation out of resonance in Figure 0.5. When the system is in resonance, light is constantly being coupled into the ring structure and only a few percent goes to the output. In a situation out of resonance, light goes directly to the output and a few percent of light (or no light at all) is coupled into the ring.

B. Effective Refractive Index Simulation of a Taper

To simulate the effective refractive index of a taper in air the Mode Analysis from COMSOL Multiphysics was used.

B.1 9 µm-Diameter Taper

A taper with 9 µm-diameter was created, with a 20 µm-diameter air surrounding. A mesh element size of wavelength/5 was used. The fundamental mode effective refractive index was calculated, searching around the refractive index of silica (n=1.444 @ 1550 nm). An effective refractive index of 1.4384 @ 1550 nm was obtained for the fundamental mode. The electric field distribution is depicted in Figure 0.6.

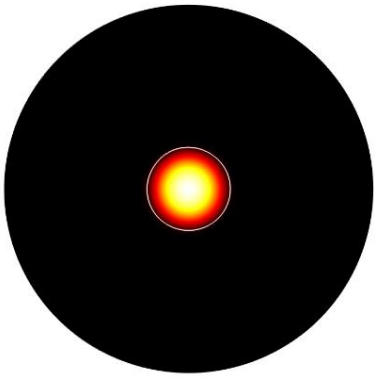

Figure 0.6. Fundamental mode of a 9 µm-diameter taper (white line).

B.2 18 µm-Diameter Taper

A taper with 18 µm-diameter was created, with a 40 µm-diameter air surrounding. A mesh element size of wavelength/5 was used. The fundamental mode effective refractive index was calculated, searching around the refractive index of silica (n=1.444 @ 1550 nm). An effective refractive index of 1.4426 @ 1550 nm was obtained for the fundamental mode. The electric field distribution is depicted in Figure 0.7a.

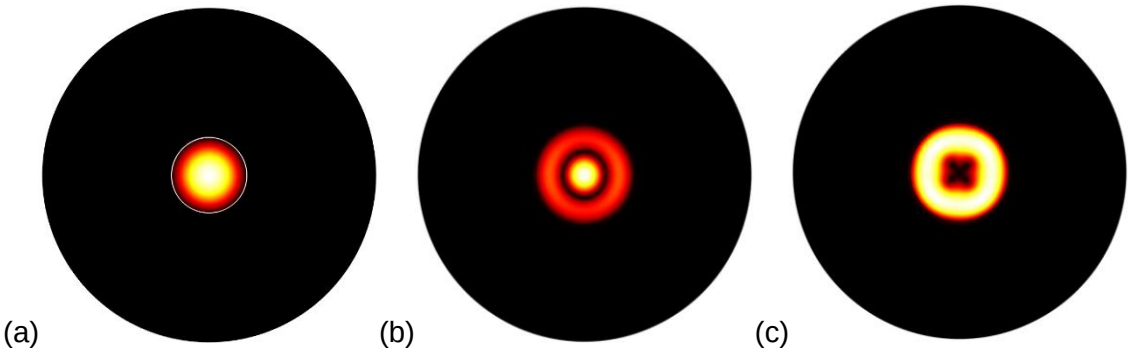

Figure 0.7. (a) Fundamental mode of an 18 µm-diameter taper (white line). (b) Higher order mode with effective refractive index 1.436343. (c) Higher order mode with effective refractive index 1.433792.

The higher mode A considered in chapter 5 has a Bragg wavelength of 1541.8 nm. Using equation (5), the effective refractive index for this mode is 1.4342. Simulating the taper modes close to this value, it is not possible to find a mode with such effective refractive index. The closest modes have an effective refractive index of 1.4363 and 1.4338, whose electric field distribution is shown in Figure 0.7 b and c respectively. In the first one, the mode is more confined to the core and in the second, the mode is predominantly in the outer part of the taper.

This deviation from the measured values can be due to a different real dimension of the taper, as well as for not counting the core which, for an 18 µm-diameter taper, has still a considerable size.

References

[1] J. Lou, Y. Wang, and L. Tong, “Microfiber optical sensors: A review,” *Sensors (Switzerland)*, vol. 14, no. 4, pp. 5823–5844, 2014.

[2] X. Wu and L. Tong, “Optical microfibers and nanofibers,” *Nanophotonics*, vol. 2, no. 5–6, pp. 407–428, 2013.

[3] G. Brambilla, F. Xu, P. Horak, Y. Jung, F. Koizumi, N. P. Sessions, E. Koukharenko, X. Feng, G. S. Murugan, J. S. Wilkinson, and D. J. Richardson, “Optical fiber nanowires and microwires: fabrication and applications,” *Adv. Opt. Photonics*, vol. 1, pp. 107–161, 2009.

[4] L. Xiao and T. a Birks, “High finesse microfiber knot resonators made from double-ended tapered fibers.,” *Opt. Lett.*, vol. 36, no. 7, pp. 1098–1100, 2011.

[5] M. Sumetsky, Y. Dulashko, J. M. Fini, A. Hale, and D. J. Digiovanni, “The Microfiber Loop Resonator : Theory , Experiment , and Application,” vol. 24, no. 1, pp. 242–250, 2006.

[6] A. Díez, M. V. Andrés, and J. L. Cruz, “In-line fiber-optic sensors based on the excitation of surface plasma modes in metal-coated tapered fibers,” *Sensors Actuators, B Chem.*, vol. 73, no. 2–3, pp. 95–99, 2001.

[7] Z. Tian, S. S. H. Yam, J. Barnes, W. Bock, P. Greig, J. M. Fraser, H. P. Loock, and R. D. Oleschuk, “Refractive index sensing with Mach-Zehnder interferometer based on concatenating two single-mode fiber tapers,” *IEEE Photonics Technol. Lett.*, vol. 20, no. 8, pp. 626–628, 2008.

[8] Z. Tian, S. S.-H. Yam, and H.-P. Loock, “Refractive index sensor based on an abrupt taper Michelson interferometer in a single-mode fiber.,” *Opt. Lett.*, vol. 33, no. 10, pp. 1105–1107, 2008.

[9] K. Q. Kieu and M. Mansuripur, “Biconical fiber taper sensors,” *IEEE Photonics Technol. Lett.*, vol. 18, no. 21, pp. 2239–2241, 2006.

[10] L. M. N. Amaral, O. Frazão, J. L. Santos, and a. B. Lobo Ribeiro, “Fiber-optic inclinometer based on taper Michelson interferometer,” *IEEE Sens. J.*, vol. 11, no. 9, pp. 1811–1814, 2011.

[11] T. Schubert, N. Haase, and H. Kück, “Refractive-index measurements using an integrated Mach-Zehnder interferometer,” *Sensors Actuators A*, vol. 60, no. 100, pp. 108–112, 1997.

[12] P. Lu, L. Men, K. Sooley, and Q. Chen, “Tapered fiber Mach-Zehnder interferometer for simultaneous measurement of refractive index and temperature,” *Appl. Phys. Lett.*, vol. 94, no. 13, pp. 3–5, 2009.

[13] L. C. Bobb, P. M. Shankar, and H. D. Krumboltz, “Bending effects in biconically tapered single-mode fibers,” *J. Light. Technol.*, vol. 8, no. 7, pp. 1084–1090, 1990.

[14] X. Ni, M. Wang, D. Guo, H. Hao, and J. Zhu, “A Hybrid Mach–Zehnder Interferometer for Refractive Index and Temperature Measurement,” *IEEE Photonics Technol. Lett.*, vol. 28, no. 17, pp. 1850–1853, Sep. 2016.

[15] S. Dass and R. Jha, “Micrometer Wire Assisted Inline Mach-Zehnder Interferometric Curvature Sensor,” *IEEE Photonics Technol. Lett.*, vol. 28, no. 1, pp. 31–34, 2016.

[16] X. Zeng, Y. Wu, C. Hou, J. Bai, and G. Yang, “A temperature sensor based on optical microfiber knot resonator,” *Opt. Commun.*, vol. 282, no. 18, pp. 3817–3819, 2009.

[17] H. Yang, S. Wang, X. Liao, and J. Wang, “Temperature Sensing in Seawater Based on Microfiber Knot Resonator,” *Sensors*, vol. 14, no. 3, pp. 18515–18525, 2014.

[18] Y. Wu, Y.-J. Rao, Y. Chen, and Y. Gong, “Miniature fiber-optic temperature sensors based on silica/polymer microfiber knot resonators,” *Opt. Express*, vol. 17, no. 20, pp. 18142–18147, 2009.

[19] K.-S. Lim, I. Aryanfar, W.-Y. Chong, Y.-K. Cheong, S. W. Harun, and H. Ahmad, “Integrated microfibre device for refractive index and temperature sensing.,” *Sensors (Basel).*, vol. 12, no. 9, pp. 11782–11789, 2012.

[20] X. Li and H. Ding, “A Stable Evanescent Field-Based Microfiber Knot Resonator Refractive Index Sensor,” *IEEE Photonics Technol. Lett.*, vol. 26, no. 16, pp. 1625–1628, 2014.

[21] Z. Xu, Q. Sun, B. Li, Y. Luo, W. Lu, D. Liu, P. P. Shum, and L. Zhan, “Highly sensitive refractive index sensor based on two cascaded microfiber knots with vernier effect,” *Opt. Express*, vol. 23, no. 5, pp. 6662–6672, 2015.

[22] H. Yu, L. Xiong, Z. Chen, Q. Li, X. Yi, Y. Ding, F. Wang, H. Lv, and Y. Ding, “Solution concentration and refractive index sensing based on polymer microfiber knot resonator,” *Appl. Phys. Express*, vol. 7, no. 2, pp. 3–7, 2014.

[23] X. Li and H. Ding, “All-fiber magnetic-field sensor based on microfiber knot

resonator and magnetic fluid.," *Opt. Lett.*, vol. 37, no. 24, pp. 5187–5189, 2012.

[24] J. M. De Freitas, T. A. Birks, and M. Rollings, "Optical micro-knot resonator hydrophone," *Opt. Express*, vol. 23, no. 5, pp. 5850–5860, 2015.

[25] M. A. Gouveia, P. E. S. Pellegrini, J. S. dos Santos, I. M. Raimundo, and C. M. B. Cordeiro, "Analysis of immersed silica optical microfiber knot resonator and its application as a moisture sensor," *Appl. Opt.*, vol. 53, no. 31, pp. 7454–7461, 2014.

[26] C.-B. Yu, Y. Wu, X.-L. Liu, B.-C. Yao, F. Fu, Y. Gong, Y.-J. Rao, and Y.-F. Chen, "Graphene oxide deposited microfiber knot resonator for gas sensing," *Opt. Mater. Express*, vol. 6, no. 3, pp. 727–733, 2016.

[27] X. Wu, F. Gu, and H. Zeng, "Palladium-Coated Silica Microfiber Knots for Enhanced Hydrogen Sensing," *IEEE Photonics Technol. Lett.*, vol. 27, no. 11, pp. 1228–1231, 2015.

[28] M. S. Yoon, S. K. Kim, and Y. G. Han, "Highly Sensitive Current Sensor Based on an Optical Microfiber Loop Resonator Incorporating Low Index Polymer Overlay," *Journal of Lightwave Technology*, vol. 33, no. 12. pp. 2386–2391, 2015.

[29] T. Ozeki and B. S. Kawasaki, "Optical directional coupler using tapered sections in multimode fibers," *Appl. Phys. Lett.*, vol. 28, no. 9, pp. 528–529, 1976.

[30] B. S. Kawasaki and K. O. Hill, "Low-loss access coupler for multimode optical fiber distribution networks.," *Appl. Opt.*, vol. 16, no. 7, pp. 1794–1795, 1977.

[31] B. S. Kawasaki, K. O. Hill, and R. G. Lamont, "Biconical-taper single-mode fiber coupler.," *Opt. Lett.*, vol. 6, no. 7, pp. 327–328, 1981.

[32] T. a. Birks and Y. W. Li, "The shape of fiber tapers," *J. Light. Technol.*, vol. 10, no. 4, pp. 432–438, 1992.

[33] J. C. Graf, S. a. Teston, P. V. De Barba, J. Dallmann, J. a S. Lima, H. J. Kalinowski, and A. S. Paterno, "Fiber taper rig using a simplified heat source and the flame-brush technique," *SBMO/IEEE MTT-S Int. Microw. Optoelectron. Conf. Proc.*, pp. 621–624, 2009.

[34] J. Shi, S. Xiao, L. Yi, and M. Bi, "A sensitivity-enhanced refractive index sensor using a single-mode thin-core fiber incorporating an abrupt taper," *Sensors*, vol. 12, pp. 4697–4705, 2012.

[35] T. E. Dimmick, G. Kakarantzas, T. a Birks, and P. S. Russell, "Carbon dioxide

laser fabrication of fused-fiber couplers and tapers.," *Appl. Opt.*, vol. 38, no. 33, pp. 6845–6848, 1999.

[36] M. Li, F. Pang, H. Guo, Y. Liu, N. Chen, Z. Chen, and T. Wang, "Tapered optical fiber fabricated by high-frequency pulsed carbon dioxide laser.," *Proc. SPIE*, vol. 7853, p. 78533E1--6, 2010.

[37] D. R. Fairbanks, "Thermal viscoelastic simulation model for tapering of laser-heated fused silica fiber," 1992, vol. 1580, pp. 188–196.

[38] A. J. C. J. C. Grellier, N. K. K. Zayer, and C. N. N. Pannell, "Heat transfer modelling in CO2 laser processing of optical fibres," *Opt. Commun.*, vol. 152, no. 4–6, pp. 324–328, 1998.

[39] F. Bayle and J.-P. Meunier, "Efficient fabrication of fused-fiber biconical taper structures by a scanned CO2 laser beam technique.," *Appl. Opt.*, vol. 44, no. 30, pp. 6402–6411, 2005.

[40] J. M. Ward, D. G. O'Shea, B. J. Shortt, M. J. Morrissey, K. Deasy, S. G. Nic Chormaic, D. G. OShea, B. J. Shortt, M. J. Morrissey, K. Deasy, and S. G. Nic Chormaic, "Heat-and-pull rig for fiber taper fabrication," *Rev. Sci. Instrum.*, vol. 77, no. 8, p. 83105, 2006.

[41] VYTRAN Datasheet, "GPX-3000 SERIES OPTICAL FIBER GLASS PROCESSORS - Glass Processing and Fusion Splicing for Standard and Large Fiber Diameters." .

[42] VYTRAN User Guide, "GPX3400 and GPX3600 Glass Processors." .

[43] M. Sumetsky, "Basic Elements for Microfiber Photonics: Micro/Nanofibers and Microfiber Coil Resonators," *J. Light. Technol.*, vol. 26, no. 1, pp. 21–27, 2008.

[44] G. Chen and M. Ding, "A review of microfiber and nanofiber based optical sensors," *Open Opt. J*, pp. 32–57, 2013.

[45] S. Lacroix, R. J. Black, C. Veilleux, and J. Lapierre, "Tapered single-mode fibers: External refractive-index dependence," *Appl. Opt.*, vol. 25, no. 15, pp. 2468–2469, 1986.

[46] W. Liang, Y. Huang, Y. Xu, R. K. Lee, and A. Yariv, "Highly sensitive fiber Bragg grating refractive index sensors," *Appl. Phys. Lett.*, vol. 86, no. 2005, pp. 1–3, 2005.

[47] T. Allsop, F. Floreani, K. P. Jedrzejewski, P. V. S. Marques, R. Romero, D. J.

Webb, and I. Bennion, “Spectral characteristics of tapered LPG device as a sensing element for refractive index and temperature,” *J. Light. Technol.*, vol. 24, no. 2, pp. 870–878, 2006.

[48] J. Wo, G. Wang, Y. Cui, Q. Sun, R. Liang, P. P. Shum, and D. Liu, “Refractive index sensor using microfiber-based Mach–Zehnder interferometer,” *Opt. Lett.*, vol. 37, no. 1, pp. 67–69, Jan. 2012.

[49] W. Tan, Z. Y. Shi, S. Smith, D. Birnbaum, and R. Kopelman, “Submicrometer intracellular chemical optical fiber sensors.,” *Science*, vol. 258, no. October, pp. 778–781, 1992.

[50] M. Belal, Z. Song, Y. Jung, G. Brambilla, and T. P. Newson, “Optical fiber microwire current sensor.,” *Opt. Lett.*, vol. 35, no. 18, pp. 3045–3047, 2010.

[51] L. Li, L. Xia, Z. Xie, and D. Liu, “All-fiber Mach-Zehnder interferometers for sensing applications,” *Opt. Express*, vol. 20, no. 10, pp. 11109–11120, 2012.

[52] H. Y. Choi, M. J. Kim, and B. H. Lee, “All-fiber Mach-Zehnder type interferometers formed in photonic crystal fiber.,” *Opt. Express*, vol. 15, no. 9, pp. 5711–5720, 2007.

[53] J. H. Lim, H. S. Jang, K. S. Lee, J. C. Kim, and B. H. Lee, “Mach-Zehnder interferometer formed in a photonic crystal fiber based on a pair of long-period fiber gratings.,” *Opt. Lett.*, vol. 29, no. 4, pp. 346–348, 2004.

[54] M. Dahlem, J. L. Santos, L. A. Ferreira, and F. M. Araujo, “Passive interrogation of low-finesse Fabry-Perot cavities using fiber Bragg gratings,” *IEEE Photonics Technol. Lett.*, vol. 13, no. 9, pp. 990–992, 2001.

[55] D. Wu, T. Zhu, M. Deng, D.-W. Duan, L.-L. Shi, J. Yao, and Y.-J. Rao, “Refractive index sensing based on Mach-Zehnder interferometer formed by three cascaded single-mode fiber tapers.,” *Appl. Opt.*, vol. 50, pp. 1548–1553, 2011.

[56] J. Yang, L. Jiang, S. Wang, B. Li, M. Wang, H. Xiao, Y. Lu, and H. Tsai, “High sensitivity of taper-based Mach-Zehnder interferometer embedded in a thinned optical fiber for refractive index sensing.,” *Appl. Opt.*, vol. 50, no. 28, pp. 5503–5507, 2011.

[57] X. Jiang, L. Tong, G. Vienne, X. Guo, A. Tsao, Q. Yang, and D. Yang, “Demonstration of optical microfiber knot resonators,” *Appl. Phys. Lett.*, vol. 88, no. 22, pp. 2004–2007, 2006.

[58] A. Kumar, T. V. B. Subrahmanyam, A. D. Sharma, K. Thyagarajan, B. P. Pal, and

I. C. Goyal, “Novel refractometer using a tapered optical fibre,” *Electron. Lett.*, vol. 20, no. 13, pp. 534–535, 1984.

[59] L. C. Bobb, H. D. Krumboltz, and P. M. Shankar, “Pressure sensor that uses bent biconically tapered single-mode fibers.,” *Opt. Lett.*, vol. 16, no. 2, pp. 112–114, 1991.

[60] O. Esteban, M. Cruz-Navarrete, a González-Cano, and E. Bernabeu, “Measurement of the degree of salinity of water with a fiber-optic sensor.,” *Appl. Opt.*, vol. 38, no. 25, pp. 5267–5271, 1999.

[61] J. Chen, B. Liu, and H. Zhang, “Review of fiber Bragg grating sensor technology,” *Front. Optoelectron. China*, vol. 4, no. 2, pp. 204–212, 2011.

[62] K. O. Hill and G. Meltz, “Fiber Bragg grating technology fundamentals and overview,” *J. Light. Technol.*, vol. 15, no. 8, pp. 1263–1276, 1997.

[63] S. P. Ugale and V. Mishra, “Modeling and characterization of fiber Bragg grating for maximum reflectivity,” *Optik (Stuttg).*, vol. 122, no. 22, pp. 1990–1993, 2011.

[64] O. Frazão, S. F. O. Silva, A. Guerreiro, J. L. Santos, L. A. Ferreira, and F. M. Araújo, “Strain sensitivity control of fiber Bragg grating structures with fused tapers,” *Appl. Opt.*, vol. 46, no. 36, pp. 8578–8582, 2007.

[65] D. a. Pereira, O. Frazão, and J. L. Santos, “Fiber Bragg grating sensing system for simultaneous measurement of salinity and temperature,” *Opt. Eng.*, vol. 43, pp. 299–304, 2004.

[66] C. J. S. De Matos, P. Torres, L. C. G. Valente, W. Margulis, and R. Stubbe, “Fiber Bragg grating (FBG) characterization and shaping by local pressure,” *J. Light. Technol.*, vol. 19, no. 8, pp. 1206–1211, 2001.

[67] Y. X. Jin, C. C. Chan, X. Y. Dong, and Y. F. Zhang, “Temperature-independent bending sensor with tilted fiber Bragg grating interacting with multimode fiber,” *Opt. Commun.*, vol. 282, no. 19, pp. 3905–3907, 2009.

[68] “Integrated Ring Resonators: The Compendium,” Berlin, Heidelberg: Springer Berlin Heidelberg, 2007, pp. 3–40.

[69] M. Becker, L. Fernandes, M. Rothhardt, S. Brückner, K. Schuster, J. Kobelke, O. Frazão, H. Bartelt, and P. V. S. Marques, “Inscription of fiber bragg grating arrays in pure silica suspended core fibers,” *IEEE Photonics Technol. Lett.*, vol. 21, no. 19, pp. 1453–1455, 2009.

[70] M. Becker, J. Bergmann, S. Brückner, M. Franke, E. Lindner, M. W. Rothhardt, and H. Bartelt, “Fiber Bragg grating inscription combining DUV sub-picosecond laser pulses and two-beam interferometry.,” *Opt. Express*, vol. 16, no. 23, pp. 19169–19178, 2008.

[71] S. Jiang, B. Zeng, Y. Liang, and B. Li, “Optical fiber sensor for tensile and compressive strain measurements by white-light Fabry-Perot interferometry,” *Opt. Eng.*, vol. 46, no. 3, pp. 34402–34402, 2007.

[72] Q. Yu and X. Zhou, “Pressure sensor based on the fiber-optic extrinsic fabry-perot interferometer,” *Photonic Sensors*, vol. 1, no. 1, pp. 72–83, 2011.

[73] W. Zheng, J. Xie, Y. Li, B. Xu, J. Kang, C. Shen, J. Wang, Y. Jin, H. Liu, K. Ni, X. Dong, C. Zhao, and S. Jin, “A fiber air-gap Fabry–Perot temperature sensor demodulated by using frequency modulated continuous wave,” *Opt. Commun.*, vol. 324, pp. 234–237, 2014.

[74] Y. J. Rao, “Recent progress in fiber-optic extrinsic Fabry-Perot interferometric sensors,” *Opt. Fiber Technol.*, vol. 12, no. 3, pp. 227–237, 2006.

[75] M. Cano-Contreras, A. D. Guzman-Chavez, R. I. Mata-Chavez, E. Vargas-Rodriguez, D. Jauregui-Vazquez, D. Claudio-Gonzalez, J. M. Estudillo-Ayala, R. Rojas-Laguna, and E. Huerta-Mascotte, “All-fiber curvature sensor based on an abrupt tapered fiber and a fabry-p??rot interferometer,” *IEEE Photonics Technol. Lett.*, vol. 26, no. 22, pp. 2213–2216, 2014.

[76] W. Yuan, F. Wang, A. Savenko, D. H. Petersen, and O. Bang, “Optical fiber milled by focused ion beam and its application for Fabry-Perot refractive index sensor,” *Rev. Sci. Instrum.*, vol. 82, no. 7, pp. 1–4, 2011.

[77] T. Wieduwilt, J. Dellith, F. Talkenberg, H. Bartelt, and M. a. Schmidt, “Reflectivity enhanced refractive index sensor based on a fiber-integrated Fabry-Perot microresonator,” *Opt. Express*, vol. 22, no. 21, pp. 25333–25346, 2014.

[78] T. Wei, Y. Han, Y. Li, H.-L. Tsai, and H. Xiao, “Temperature-insensitive miniaturized fiber inline Fabry-Perot interferometer for highly sensitive refractive index measurement.,” *Opt. Express*, vol. 16, no. 8, pp. 5764–5769, 2008.

[79] C. R. Liao, T. Y. Hu, and D. N. Wang, “Optical fiber Fabry-Perot interferometer cavity fabricated by femtosecond laser micromachining and fusion splicing for refractive index sensing,” *Opt. Express*, vol. 20, no. 20, p. 22813, 2012.

[80] T. Wei, Y. Han, H.-L. Tsai, and H. Xiao, “Miniaturized fiber inline Fabry-Perot

interferometer fabricated with a femtosecond laser.," *Opt. Lett.*, vol. 33, no. 6, pp. 536–538, 2008.

[81] M. L. von Bibra, A. Roberts, and J. Canning, "Fabrication of long-period fiber gratings by use of focused ion-beam irradiation.," *Opt. Lett.*, vol. 26, no. 11, pp. 765–767, 2001.

[82] J. Feng, M. Ding, J. L. Kou, F. Xu, and Y. Q. Lu, "An optical fiber tip micrograting thermometer," *IEEE Photonics J.*, vol. 3, no. 5, pp. 810–814, 2011.

[83] F. Le Kien, K. P. Nayak, and K. Hakuta, "Nanofibers with Bragg gratings from equidistant holes," *Opt. Express*, vol. 19, no. 15, pp. 200–203, 2011.

[84] C. Martelli, P. Olivero, J. Canning, N. Groothoff, B. Gibson, and S. Huntington, "Micromachining structured optical fibers using focused ion beam milling.," *Opt. Lett.*, vol. 32, no. 11, pp. 1575–1577, 2007.

[85] S. C. Warren-Smith, R. M. André, C. Perrella, J. Dellith, M. Rothhardt, and H. Bartelt, "Direct core structuring of microstructures optical fibers using focused ion beam milling," *Opt. Express*, vol. 24, no. 1, pp. 854–858, 2015.

[86] J. Kou, J. Feng, Q. Wang, F. Xu, and Y. Lu, "Microfiber-probe-based ultrasmall interferometric sensor.," *Opt. Lett.*, vol. 35, no. 13, pp. 2308–2310, 2010.

[87] J. Kou, J. Feng, L. Ye, F. Xu, and Y. Lu, "Miniaturized fiber taper reflective interferometer for high temperature measurement.," *Opt. Express*, vol. 18, no. 13, pp. 14245–14250, 2010.

[88] R. M. André, S. Pevec, M. Becker, J. Dellith, M. Rothhardt, M. B. Marques, D. Donlagic, H. Bartelt, and O. Frazão, "Focused ion beam post-processing of optical fiber Fabry-Perot cavities for sensing applications.," *Opt. Express*, vol. 22, no. 11, pp. 13102–13108, 2014.

[89] P. Sigmund, "Theory of Sputtering. I. Sputtering Yield of Amorphous and Polycrystalline Targets," *Phys. Rev.*, vol. 184, no. 2, pp. 383–416, Aug. 1969.

[90] S. Reyntjens and R. Puers, "A review of focused ion beam applications in microsystem technology," *J. Micromechanics Microengineering*, vol. 11, no. 4, pp. 287–300, 2001.

[91] G. Meltz, S. J. Hewlett, and J. D. Love, "Fiber grating evanescent-wave sensors," 1996, vol. 2836, pp. 342–350.

[92] R. A. Asseh, S. Sandgren, H. Ahlfeldt, B. Sahlgren and G. E. Stubbe, "Fiber

Optical Bragg Grating Refractometer," *Fiber Integr. Opt.*, vol. 17, no. 1, pp. 51–62, 1998.

[93] K. Zhou, Z. Yan, L. Zhang, and I. Bennion, "Refractometer based on fiber Bragg grating Fabry-Pérot cavity embedded with a narrow microchannel," *Opt. Express*, vol. 19, no. 12, pp. 11769–11779, 2011.

[94] M. C. Phan Huy, G. Laffont, V. Dewynter, P. Ferdinand, P. Roy, J.-L. Auguste, D. Pagnoux, W. Blanc, and B. Dussardier, "Three-hole microstructured optical fiber for efficient fiber Bragg grating refractometer.," *Opt. Lett.*, vol. 32, no. 16, pp. 2390–2392, 2007.

[95] M. C. Phan Huy, G. Laffont, V. Dewynter, P. Ferdinand, L. Labonté, D. Pagnoux, P. Roy, W. Blanc, and B. Dussardier, "Tilted Fiber Bragg Grating photowritten in microstructured optical fiber for improved refractive index measurement.," *Opt. Express*, vol. 14, no. 22, pp. 10359–10370, 2006.

[96] S. C. Warren-Smith and T. M. Monro, "Exposed core microstructured optical fiber Bragg gratings: refractive index sensing.," *Opt. Express*, vol. 22, no. 2, pp. 1480–1489, 2014.

[97] Y. Liu, C. Meng, a P. Zhang, Y. Xiao, H. Yu, and L. Tong, "Compact microfiber Bragg gratings with high-index contrast.," *Opt. Lett.*, vol. 36, no. 16, pp. 3115–3117, 2011.

[98] W. Jin, G. Thursby, M. Konstantaki, and B. Culshaw, "Simultaneous measurement of strain and temperature: error analysis," *Opt. Eng.*, vol. 36, no. 2, pp. 598–609, 1997.

[99] Y. Ran, L. Jin, L. Sun, J. Li, and B. Guan, "Temperature-Compensated Refractive-Index Sensing Using a Single Bragg Grating in an Abrupt Fiber Taper," *IEEE Photonics J.*, vol. 5, no. 2, pp. 7100208–7100208, 2013.

[100] A. D. Gomes and O. Frazão, "Mach – Zehnder Based on Large Knot Fiber Resonator for Refractive Index Measurement," *IEEE Photonics Technol. Lett.*, vol. 28, no. 12, pp. 1279–1281, Jun. 2016.

[101] Y. Liu, M. Li, H. Sun, Y. Li, and S. Qu, "Ultrasensitive liquid refractometer based on a Mach-Zehnder micro-cavity in optical fibre fabricated by femtosecond laser-induced water breakdown," *J. Mod. Opt.*, vol. 340, no. July, pp. 1–6, 2016.

[102] K. S. Lim, A. a Jasim, S. S. a Damanhuri, S. W. Harun, B. M. A. Rahman, and H. Ahmad, "Resonance condition of a microfiber knot resonator immersed in liquids.,"

Appl. Opt., vol. 50, no. 30, pp. 5912–5916, 2011.

[103] Comsol, “Optical Ring Resonator Notch Filter (Solved with COMSOL Multiphysics 5.1).” p. 24.